SANDIA REPORT
SAND2001-2619
Unlimited Release
Printed September 2001

Multicomponent-Multiphase Equation of State for Carbon

Gerald I. Kerley and Lalit Chhabildas

Prepared by
Sandia National Laboratories
Albuquerque, New Mexico 87185 and Livermore, California 94550

Sandia is a multiprogram laboratory operated by Sandia Corporation,
a Lockheed Martin Company, for the United States Department of
Energy under Contract DE-AC04-94AL85000.

Sandia National Laboratories

Issued by Sandia National Laboratories, operated for the United States Department of Energy by Sandia Corporation.

Available to DOE and DOE contractors from
U.S. Department of Energy
Office of Scientific and Technical Information
P.O. Box 62
Oak Ridge, TN 37831

Telephone: (865)576-8401
Facsimile: (865)576-5728
E-Mail: reports@adonis.osti.gov
Online ordering: http://www.doe.gov/bridge

Available to the public from
U.S. Department of Commerce
National Technical Information Service
5285 Port Royal Rd
Springfield, VA 22161

Telephone: (800)553-6847
Facsimile: (703)605-6900
E-Mail: orders@ntis.fedworld.gov
Online order: http://www.ntis.gov/ordering.htm

SAND2001-2619
Unlimited Release
Printed September 2001

Multicomponent-Multiphase Equation of State for Carbon

Gerald I. Kerley, Consultant
Kerley Technical Services
P.O. Box 709
Appomattox, VA 24522-0709

Lalit C. Chhabildas
Shock Physics Applications Department
Sandia National Laboratories,
P.O. Box 5800
Albuquerque, NM 87185-1181

Abstract

The PANDA code is used to build a tabular equation of state (EOS) table for carbon. The model includes three solid phases (graphite, diamond, and metallic) and a fluid phase mixture containing three molecular components (C_1, C_2, and C_3). Separate EOS tables were first constructed for each solid phase and for each molecular species in the fluid phase. Next, a mixture/chemical equilibrium model was used to construct a single multicomponent EOS table for the fluid phase from those for the individual chemical species. Finally, the phase diagram and multiphase EOS were determined from the Helmholtz free energies. The model gives good agreement with experimental thermophysical data, static compression data, known phase boundaries, and shock-wave measurements. This EOS covers a wide range of densities (0 - 100 g/cm^3) and temperatures (0 - 1.0×10^{8}K). The new EOS table can be accessed through the SNL-SESAME library as material number 7830.

Contents

Figures

Symbols and Units

ρ	density [g/cm^3]
V	specific volume, $V = 1/\rho$ [cm^3/g]
T	temperature [*K*]
P	pressure [*GPa*]
E	specific internal energy [*MJ/kg*]
A	Helmholtz free energy [*MJ/kg*]
S	entropy [*MJ/(kg-K)*]
β	isothermal bulk modulus, $\beta = \rho(\partial P/\partial \rho)_T$ [*GPa*]
E_B	cohesive energy of solid at zero pressure and temperature [*MJ/kg*]
ρ_0	density of solid at zero pressure and temperature [g/cm^3]
β_0	bulk modulus of solid at zero pressure and temperature [*GPa*]
C_S	sound velocity [*km/s*]
U_S	shock velocity [*km/s*]
u_P	particle velocity [*km/s*]
R	gas constant [8.31451×10^{-3} *MJ/kg-mole-K*]
W	atomic or molecular weight [*g/mole*]
k	Boltzmann’s constant [1.38066×10^{-29} *MJ/K*]

1. Introduction

1.1 Background

The unique properties of carbon have made it both a fascinating and an important subject of experimental and theoretical studies for many years [1]-[4]. The contrast between its best-known elemental forms, graphite and diamond, is particularly striking. Graphite is black, has a rather low density and high compressibility (close to that of magnesium), and is greasy enough to be useful as a lubricant and in pencil leads. Diamond is brilliantly translucent, 60% more dense than graphite, less compressible than either tungsten or corundum, and its hardness makes it useful for polishing and cutting. This variability in properties, as well as that observed among the many classes of carbon compounds, arises because of profound differences in electronic structure of the carbon bonds [5].

A number of other solid forms of carbon are known. Pyrolytic graphite [6] is a polycrystalline material in which the individual crystallites have a structure quite similar to that of natural graphite. Fullerite (solid C_{60}), discovered only ten years ago [7], consists of giant molecules in which the atoms are arranged into pentagons and hexagons on the surface of a spherical cage. Amorphous carbon [8][9], including carbon black and ordinary soot, is a disordered form of graphite in which the hexagonally bonded layers are randomly oriented. Glassy carbons [9][10], on the other hand, have more random structures. Many other structures have been discussed [1][9].

Because of its high melting point, low thermal expansion, and high heat capacity, graphite is often used in structural materials and composites, as in heat shields for space reentry vehicles. In addition to its importance as a pure material, there has been considerable interest in carbon because of its formation in the detonation products of explosives and in the decomposition products of hydrocarbons, plastics, and other compounds [11]-[13].

The carbon phase diagram exhibits some interesting features, some of which are still not completely understood. In the numerical simulation of dynamic phenomena, it is important to account for the phase transition from graphite to diamond. However, this transition does not occur at the equilibrium pressure in shock-wave experiments. While a full non-equilibrium model of this transition is not yet available, we have shown that many aspects of the behavior can be reproduced by treating diamond as an imperfect crystal [11][12].

The high melting point has limited experimental investigations of the liquid phase, but some information has been obtained using dynamic methods. A recent discussion of the methods and their difficulties is given by Musella, et al. [14]. The graphite-liquid boundary is known to exhibit a temperature maximum at about 5-6 GPa [15]. This feature shows that liquid carbon is less dense than graphite at low pressure but becomes denser as the pressure is increased, indicating a rather significant change in compressibility. The conductivity of liquid carbon also depends upon pressure—insulating behavior is observed at low pressures, metallic behavior at higher pressures.

Carbon does not vaporize at atmospheric pressure; it sublimes at a temperature below the graphite-liquid-vapor triple point [14]. Analysis of the sublimation data shows that polyatomic molecules are present in the vapor [16][17].

1.2 Scope of Work

In this work, we use the PANDA code [18] to construct a multicomponent-multiphase EOS model for carbon that is valid over a wide range of densities and temperatures. The results are put into tabular form for use in numerical simulations using the Sandia hydrocode CTH and other codes utilizing the SESAME format [19]-[23].

The model includes three solid phases—graphite, diamond, and metallic solid. Two models are created for diamond—the perfect crystal, used to compute the equilibrium properties, and an imperfect form, used to describe nonequilibrium behavior. The solid models are discussed in Section 2.

Our model for the fluid phase (liquid, vapor, and supercritical regions) allows for the existence of several chemical species—the monatomic form C_1, which is metallic, and the polyatomic molecules C_2, C_3, C_4, and C_5. The PANDA mixture-chemical equilibrium model is used to construct a single EOS for the fluid phase. C_3 molecules are shown to be important, not only in the vapor phase, but also in the liquid phase at low pressures. The transition from C_3 to C_1 under pressure is found to explain the distinctive character of the graphite-melting curve. The liquid models are discussed in Section 3.

The models for the metallic solid and liquid also include contributions from thermal electronic excitation and ionization, which become very important at high temperatures. These contributions were calculated using the PANDA ionization equilibrium model. The version used here, which contains some new features that were not discussed in the original PANDA manual, is described in Section 4.

Results of the model are discussed in Section 5. Good agreement is obtained with a variety of experimental information—the phase diagram, shock-wave data, including shock-induced phase transitions, isobaric expansion, sound speed in the shocked state, and shock-vaporization experiments.

Conclusions and recommendations are given in Section 6.

2. EOS for Solid Phases

2.1 General

We will consider three solid phases of carbon in this work—graphite, diamond, and metallic. We will also consider an imperfect form of diamond, used in treating deviations from the equilibrium phase diagram. The thermodynamic functions for the solid phases are expressed as sums of four terms that are assumed to be separable and additive:

$$P(\rho, T) = P_c(\rho) + P_l(\rho, T) + P_e(\rho, T), \tag{1}$$

$$E(\rho, T) = E_c(\rho) + E_l(\rho, T) + E_e(\rho, T) - \Delta E_b, \tag{2}$$

$$A(\rho, T) = E_c(\rho) + A_l(\rho, T) + A_e(\rho, T) - \Delta E_b. \tag{3}$$

The subscripts c and l denote contributions from the zero-Kelvin curve and lattice vibrations, respectively. The subscript e denotes the contributions from thermal electronic excitations, which were included only for the metallic phase; this term is discussed in Section 2.3. In order to give a consistent energy zero for all three phases, the constants ΔE_b were chosen according to

$$\Delta E_b = [E_c(\rho_{298}) + A_l(\rho_{298}, 298) + A_e(\rho_{298}, 298)] - \Delta H_f^o(298), \tag{4}$$

where ρ_{298} is the density of the phase at 298K and ambient pressure, and $\Delta H_f^o(298)$ is its enthalpy of formation relative to graphite.

The zero-Kelvin curves were fit to the Birch-Murnaghan equation [24],

$$P_c(\rho) = \frac{3}{2}\beta_0(\eta^{7/3} - \eta^{5/3})\left[1 + \frac{3}{4}(\eta^{2/3} - 1)(\beta'_0 - 4)\right], \tag{5}$$

$$E_c(\rho) = \frac{9\beta_0}{8\rho_0}(\eta^{2/3} - 1)^2\left[\frac{1}{2}(\eta^{2/3} - 1)(\beta'_0 - 4) + 1\right], \tag{6}$$

where $\eta = \rho/\rho_0$, and ρ_0, β_0, and β'_0 are constants. To insure correct asymptotic behavior at high densities, the PANDA extrapolation formula [18], which is based on Thomas-Fermi-Dirac (TFD) theory, was used at high pressures.

The lattice-vibrational terms were computed using the well-known Debye and Einstein models. The equations for these models are given in the PANDA manual [18], and we will limit the present discussion to points specific to carbon.

2.2 Graphite

The cold curve parameters for graphite were determined by fitting ultrasonic data [6], static compression data [25], and shock wave data [26]-[29], including contributions from the lattice vibrations, discussed below. Our room temperature (RT) isotherm and Hugoniot are compared with the experimental data in Figure 1. The two curves are almost indistinguishable at pressures below 35 GPa. The static data extend to 14 GPa. The shock data for all forms of graphite, except those for pyrolytic graphite, are in good agreement with the static data and show the onset of transition to diamond at about 2 0GPa.

The data for pyrolytic graphite are higher in stress by about 2 GPa, evidently due to strength. As shown in Figure 1, these data agree with the other data when shifted by -2 GPa. In the earlier shock experiments [26][27], pyrolytic graphite did not transform to diamond at pressures below about 35 GPa. Data that are more recent show that the transformation that occurs at 20 GPa when high-quality pyrolytic graphite is used and the shock pressure is applied perpendicular to the basal plane [28][29].

After accounting for thermal and strength effects, we obtain the following cold curve parameters for graphite: $\rho_0 = 2.293$, $\beta_0 = 38.2$, and $\beta'_0 = 11.0$. This fit is valid up to at least 35 Pa, covering the entire region of stability. The TFD extrapolation formula [18] was used to define the cold curve in the metastable region at higher pressures.

Figure 1. Compression curves for solid carbon phases. Experimental data: circles—RT isotherm for graphite [25]; x's—Hugoniot data for graphite; crosses—Hugoniot data for pyrolytic graphite, shifted by -2 GPa; diamonds—RT isotherm for diamond [30]. Theoretical curves: solid—RT isotherm for graphite; dotted—Hugoniot for graphite; long dash—RT isotherm for diamond; short dash—0K isotherm for diamond; dotdash—RT isotherm for metallic solid.

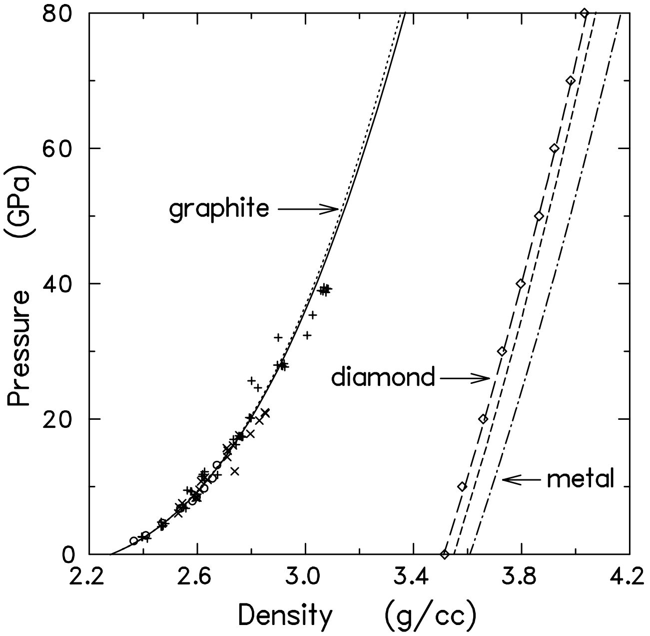

Our model for the lattice vibrational modes of graphite is based upon the theoretical work of Al-Jishi and G. Dresselhaus [31]. They calculated the lattice vibrational spectrum using the Born-von Kármán model with 4 atoms per unit cell, a total of 12 vibrational modes.

We treated nine of these modes as Einstein oscillators, with frequencies corresponding to the peaks in their calculated spectrum. The other three modes were treated using the Debye model, with the Debye temperature chosen to match the experimental entropy as a function of temperature. Our model gives an idealized, but reasonable representation of the integrated density of states obtained from the calculations of Reference [31]. For the lowest frequency Einstein mode, thermal softening was included in order to match the entropy at high temperatures [16], and the mode Grüneisen parameter was chosen to match the thermal expansion of pyrolytic graphite [32]. The other frequencies were taken to be constant.

Our calculations of the entropy and density vs. temperature, at zero pressure, are compared with the experimental data in Figures 2 and 3, respectively.

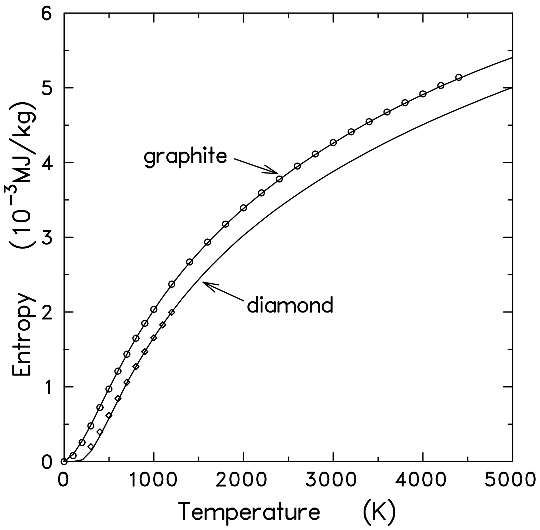

Figure 2. Entropy vs. temperature for graphite and diamond. Experimental data are from [16] and [33]. Solid curves are calculated from model.

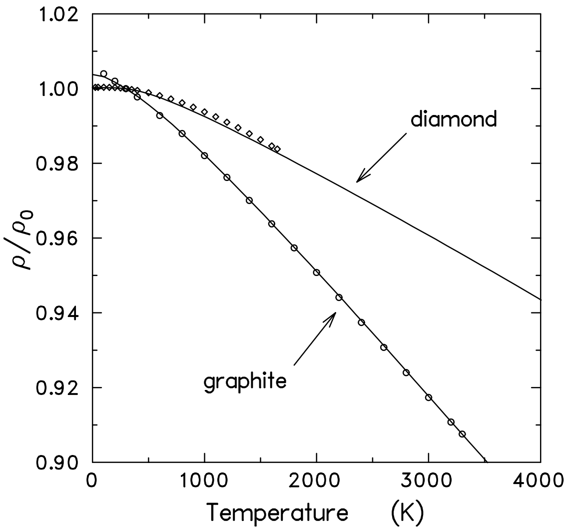

Figure 3. Density vs. temperature for graphite and diamond. Experimental data are from [32]. Solid curves are calculated from model.

The heat of formation for graphite is zero by definition.

2.3 Diamond

The cold curve parameters for diamond were determined by fitting the calculations of Fahy and Louie [34], with a small correction to match the ambient density [35] and sound speed [36]. The result is: $\rho_0 = 3.550$, $\beta_0 = 452.0$, and β'_0 3.64. The TFD extrapolation was used above a density of 4.5 g/cm^3 (about 100 GPa).

Our room temperature isotherm is compared with the static compression data of Aleksandrov, et al. [30] in Figure 1. Our fit is in good agreement with the data—provided their corrections for the calibration scale is included. (See Figure 6 of Reference [30].) The calibration corrections are particularly important above about 40GPa.

Diamond is a classic example of the single-oscillator Einstein model of the specific heat [37]. We have used the Einstein model to compute the lattice vibrational contributions, with an Einstein temperature of 1320K as in the original work, and a Grüneisen parameter of 0.96, as determined from measurements of the pressure dependence of the Raman mode [38]. Our calculations of the entropy and density vs. temperature, at zero pressure, are compared with the experimental measurements of the entropy vs. temperature [33] and the thermal expansion [32] in Figures 2 and 3, respectively. The calculated results are in good agreement with the data.

The heat of formation of diamond is $\Delta H_f^o(298)$ = 0.158 MJ/kg [39].

2.4 An Imperfect Form of Diamond

The above EOS model corresponds to the perfect crystalline form of diamond. This model, together with our EOS for graphite, gives good results for the graphite-diamond phase line, as we will show in Section 5.2.

However, shock wave data for carbon show that the transition from graphite to diamond occurs at about 10 times the equilibrium transition pressure. In addition, the high-density phase is found to be about 5% less dense than shocked diamond [29]. Only part of this density difference can be attributed to thermal effects, i.e., the higher temperature obtained by shocking from the lower initial density of graphite.

A full treatment of these nonequilibrium effects would require a time-dependent model. However, we have shown than much of the observed behavior can be reproduced by treating the high-density phase as an imperfect form of diamond [11]. It is reasonable to expect that the diamond produced on the time scale of a shock wave experiment would have a large number of imperfections—vacancies, dislocations, grain boundaries, etc.. For simplicity, we will treat these imperfections as vacancies. Because the energy difference between graphite and diamond is small compared to the carbon bond energy, a small percentage of vacant sites in the diamond lattice can increase the transition pressure by an order of magnitude while simultaneously reducing the density. Ultrafine diamonds, which have a large ratio of surface area to volume, would exhibit the same effect.

Our EOS for this imperfect form of diamond was constructed using the PANDA vacancy model [18]. It is assumed that a certain fraction of the lattice sites, $0 \le f_v \le 1$, are vacant. The presence of these vacancies lowers the density of the solid from its ideal value and reduces the effective binding of the solid lattice. The energy and pressure on the cold curve are modified as follows.

$$E_c(\rho) \rightarrow (1 - f_v) E_c[(1 + f_v)\rho], \tag{7}$$

$$P_c(\rho) \to (1 - f_v) P_c[(1 + f_v)\rho] / (1 + f_v)\,. \qquad (8)$$

The vacancies also make a contribution to the entropy, which is computed by assuming the vacant sites to be randomly distributed. The result is

$$\Delta S_{vac} = -R[f_v \ln f_v / (1 - f_v) + \ln(1 - f_v)] / W, \qquad (9)$$

where R is the gas constant and W is the atomic weight.

In the present work, we find that assuming only 3% of the sites to be vacant ($f_v = 0.03$) gives satisfactory agreement with the shock data.

2.5 Metallic Solid

Simple theoretical arguments, together with analogy to the other Group IVA elements (Si, Ge, Sn, and Pb), indicate that carbon should transform to a metallic phase at sufficiently high pressures. However, the transition pressure and structure of this phase have not been established experimentally. There could even be more than one high-pressure phase transition.

Theoretical calculations have been made for many different structures [34][40]-[43]. Of all that have been considered, the fourfold coordinated structure bc-8 (or Si-III) is by far the most stable energetically [34]. The sixfold coordinated structures (sc and β-Sn) are higher in energy and also kinetically unstable. The most highly coordinated structures (fcc, bcc, hcp) are highest in energy.

We assume that the metallic phase is bc-8 in this work. The cold curve parameters were determined by fitting the calculations of Fahy and Louie [34]. The result is: $\rho_0 = 3.656$, $\beta_0 = 440$, and $\beta'_0 = 3.7$. (Our value of β_0 differs slightly from that given by Fahy and Louie, who used a different formula to fit the EOS in the region near zero pressure.) The TFD extrapolation was used above a density of 4.5 g/cm^3 (about 100 GPa). Our room temperature isotherm for the metallic phase is shown in Figure 1.

The lattice vibrational contributions for the bc-8 phase were calculated using the Debye model. In the absence of experimental data, the Debye temperature Θ was estimated from the sound speed, using the Slater formula with a Poisson’s ratio of 1/3 (Equation 2.1 of Reference [18]); the result was $\Theta = 1270$K. The Grüneisen parameter Γ was estimated from the cold curve, using the Dugdale-MacDonald formula (Equation 4.19 of Reference [18]); the result was $\Gamma = 1.35$.

The electronic terms in Equations. (1)-(3) were computed from the ionization equilibrium model discussed in Section 4.

Fahy and Louie also predicted that the energy of the bc-8 phase is higher than that of diamond by 5.5 MJ/kg. After correcting for thermal and zero-point energy terms, we obtain a heat of formation $\Delta H_f^o(298)$ of 5.3 MJ/kg for the bc-8 phase.

As we will show in Section 3.3, the bct-8 cold curve is also used in our model for the monatomic liquid phase. Equations (5) and (6) only define the cold curve in the compression region. The LJ MATCH option in PANDA was used to define the tension region, which is needed for the liquid model. In order to insure the correct value of the binding energy E_B as the density approaches zero, the energy on the cold curve is represented by [18]

$$E_c(\rho) = f_1\rho^{f_2} - f_3\rho^{f_{LJ}} + E_B \text{ for } \rho \le \rho_{LJ}. \tag{10}$$

This option requires three parameters—E_B, ρ_{LJ}, and f_{LJ}. (f_1, f_2, and f_3 are determined by requiring that the energy, pressure, and first derivative of the pressure are continuous at the match density.)

The binding energy was determined from the heat of formation for the bct-8 phase and that for carbon gas [39], along with thermal and zero-point energy corrections. The result was E_B = 55.0 MJ/kg. Values for the other two parameters, which are less critical, were obtained from those we previously obtained for iron [44], by scaling according to density: ρ_{LJ} = 3.25, f_{LJ} = 0.75.

3. EOS for Fluid Phase

3.1 General

Our EOS for the fluid phase—which includes the liquid, gas, and supercritical regions—allows for the existence of several molecular species (C_n, n=1,2,3,...). The EOS for each species is calculated using the PANDA liquid model [18]. The Helmholtz free energy has the form

$$A(\rho, T) = A_\phi(\rho, T) + A_{vr}(\rho, T) + A_e(\rho, T) - \Delta E_b . \tag{11}$$

Here A_ϕ includes the contributions from the intermolecular forces and the thermal motions of the molecular centers of mass. A_{vr} is the contribution from internal rotational and vibrational degrees of freedom, included only for the polyatomic species. A_e is the contribution from thermal electronic excitations, included only for the monatomic and diatomic species. The constants ΔE_b were chosen to give the same energy zero as for the solid phases. The other thermodynamic quantities were computed from the usual thermodynamic relations.

After separate EOS tables have been constructed for each chemical species, the PANDA mixture model is used to construct an EOS for the complete system. This model employs the ideal mixing approximation—the mixture components have equal temperatures and pressures, their volumes are additive, and the entropy of mixing is that for complete randomness. The chemical composition is computed from the principle of chemical equilibrium, i.e., by minimizing the free energy. Hence, the molecular composition varies with density and temperature.

3.2 Liquid Perturbation Theory

The first term in Eq. (11), A_ϕ, was calculated using a version of liquid perturbation theory called the CRIS model [45][46]. This model has been discussed in detail in previous work, and we will review only a few points here.

The thermodynamic properties of a fluid are determined by the potential energy ϕ of a molecule in the field of neighboring molecules. The free energy A_ϕ can be written in terms of this function by using a perturbation expansion about the properties of an idealized hard-sphere fluid,

$$A_\phi(\rho, T) = A_0(\rho, T, \sigma) + (N_0/W)\langle\phi\rangle_0 + \Delta A , \tag{12}$$

where N_0 is Avogadro's number and W is the molecular weight. Here A_0 is the free energy for a fluid of hard spheres with diameter σ, and $\langle\phi\rangle_0$, the first-order correction, is an average of ϕ over all configurations of the hard sphere fluid. In the CRIS model, the hard-sphere diameter σ is defined by a variational principle that minimizes $|\Delta A|$, where ΔA includes all corrections to the first two terms. This approach defines the hard-sphere system having a structure that is closest to that of the real fluid. The corrections are then computed from approximate expressions.

The function ϕ depends upon the intermolecular forces and is related to the zero-Kelvin energy of the solid phase by

$$E_c(\rho) = (N_0/W)\phi(\mathbf{x}_s), \tag{13}$$

where $\mathbf{x}_s$ denotes the configuration of the neighbors in the solid at density ρ. To calculate the fluid properties from Eq. (12), ϕ must be averaged over many configurations of neighbors that are different from those of the solid. Since current theories of the electronic structure of matter are not sufficiently accurate for calculating ϕ, except for very simple systems, the CRIS model idealizes the fluid configurations and approximates ϕ by

$$\phi \approx (\rho/\rho_s)E_c(\rho_s) \tag{14}$$

Here ρ is the actual density of the fluid, and ρ_s is the solid density having the same nearest neighbor distance as that of the given fluid configuration. For this approximation to be valid, the short-range structure of the solid must be reasonably close to that in the liquid. When several solid structures are possible, one must choose the one that gives the best results for the liquid or adjust the cold curve to fit the data.

3.3 Monatomic Fluid Species (C_1)

Since theoretical calculations show that the properties of solid carbon vary markedly with structure, there is ambiguity as to which cold curve E_c to use in the model for monatomic fluid carbon. However, the fact that liquid carbon exhibits metallic conductivity at pressures above ~5 GPa [4] suggests that the cold curve for a metallic solid structure should be used. Of all the structures that have been studied theoretically, only bc-8 has a binding energy of the right magnitude to reproduce the observed melting point when used with the fluid model. In this work, therefore, we have used the same function E_c for the C_1 fluid as for the bc-8 phase, discussed in Section 2.5. As a result, the energy shift ΔE_b is also the same as for the bc-8 phase.

As in previous work on liquid metals, the EFAC energy parameter in the CRIS model was used to “fine tune” the results. We set EFAC = 1.45 MJ/kg (2.6% of the cohesive energy) to match the graphite melting line at high pressures (Section 5.2). As noted in Section 2.5, two parameters in the PANDA LJMATCH option, which defines the behavior of the zero-Kelvin isotherm in tension, were estimated from those for iron [44].

The thermal electronic term for the C_1 fluid, which is the same as that for the bc-8 solid, is discussed in Section 4. $A_{vr} = 0$ for monatomic carbon, since it has no internal degrees of freedom.

3.4 Polyatomic Fluid Species (C_n)

Calculations using our EOS for the C_1 fluid, together with the graphite and diamond EOS, give good agreement with experimental data at high pressures. In particular, it reproduces the negative slope of the graphite melting curve above 6 GPa and the shock data that lie in the liquid region (Section 5.2). At low pressures, the positive slope of the graphite melting curve shows that the liquid is less dense than graphite, which is inconsistent with our model for the C_1 fluid. The conductivity of the liquid also decreases at low pressures [4][14]. These observations indicate a significant change in the liquid structure at low pressures. Good agreement with the low-pressure data can be obtained when polyatomic molecules are allowed to form in the liquid.

In calculating thermodynamic properties for the polyatomic species, Eq. (11), the C_n molecules were treated as freely rotating, and hence spherically symmetric, in computing the contributions from center-of-mass motion, A_ϕ. Contributions from the internal rotations and vibrations, A_{vr}, were computed using the rigid rotator-harmonic oscillator approximation [18], with parameters taken from the JANAF Tables [16]. For C_2, the thermal electronic term A_e was also calculated from the energy and degeneracy of the lowest-lying excited state [16][18]. The energy shifts ΔE_b were determined from the gas-phase heats of formation [16]. Since all of these parameters can be fixed rather easily, the only challenge is to determine the cold curves needed by the liquid model, for computing A_ϕ

There are no direct experimental measurements of the cold curves or intermolecular forces for C_n molecules, and first-principles quantum-mechanical calculations are beyond the scope of this report—probably beyond the present state of the art. Therefore, we will have to estimate the cold curves using simple, semi-empirical arguments. As we will show, these arguments demonstrate that C_3 is the only important polyatomic species in the liquid phase.

Given the lack of information, it is desirable to minimize the number of parameters used in the model as much as possible. With this end in mind, the cold curves were represented using the so-called "universal" formula of Rose, et al. [47]. In PANDA, this expression is written in the form [18]

$$E_c(\rho_s) = E_B - E_B(1 + a + 0.05a^3)exp(-a), \tag{15}$$

$$P_c(\rho_s) = -\sqrt{\beta_0 E_B / \rho_0}\,(\rho_0/\rho_s)^{1/3}\rho_s(a - 0.15a^2 + 0.05a^3)exp(-a), \tag{16}$$

where

$$a = 3\sqrt{\beta_0/\rho_0 E_B}\,[(\rho_0/\rho_s)^{1/3} - 1]. \qquad (17)$$

Here E_B, ρ_0, and β_0 are the cohesive energy, density, and bulk modulus of the condensed phase at zero pressure. These parameters were further restricted by requiring that, for given values of E_B and ρ_0, β_0 be chosen to make Eq. (16) extrapolate smoothly into the TFD curve at high pressures. This additional constraint defines a family of cold curves for the various C_n species, determined only by the two parameters E_B and ρ_0

In order to estimate values for the parameters E_B and ρ_0, we consider next the electronic structure of a C_n molecule, which has been studied by Pitzer and Clementi [17]. They showed that a conventional chemical valence picture of the bonding is

$$:\mathrm{C{=}C{=}C}\cdots\mathrm{C{=}C}:$$

The molecules are linear, the carbon atoms are doubly bonded (one σ- and one π-bond), and each of the terminal carbon atoms has an unbonded electron pair. In further support of this picture, we note that the average bond energies, calculated from the heats of formation [16], are as follows: C_2 - 594 kJ, C_3 - 661 kJ, C_4 - 624 kJ, C_5 - 640 kJ. These values are in good agreement with the typical C-C double bond energy (615 kJ, compared with 347 for a single bond and 812 for a triple bond [5]).

For purposes of comparison, N_2, O_2, and CO_2 have the following structures:

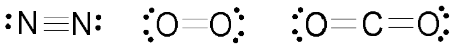

$$:\mathrm{N{\equiv}N}: \qquad \mathrm{O{=}O} \qquad \mathrm{O{=}C{=}O}$$

The intermolecular forces in these three compounds are due primarily to interactions between the terminal electrons and the π-electron groups with those on neighboring molecules. We have previously obtained values of E_B in the range 0.3-0.4 MJ/kg for these compounds. Sensitivity studies demonstrate that such values are much too small to allow formation of C_n molecules in the liquid state.

However, the electronic structure of a C_n molecule differs from that of N_2, O_2, and CO_2 in a very important way—the terminal carbon atoms in C_n are deficient in electrons. Each terminal carbon is capable of forming two additional covalent bonds, as in the interior of the chain, or interacting with surrounding molecules by metallic bonding (delocalized electrons). There should be an especially large contribution to the interaction energy from neighboring molecules aligned along the same axis.

Define ε_n to be the average energy of interaction of a C_n molecule with its neighbors. Each atom in the chain will have an energy ε_p in the four directions perpendicular to the axis. Each terminal atom will also have an energy ε_t in the parallel direction. Hence

$$\varepsilon_n \approx (1/2)(4n\varepsilon_p + 2\varepsilon_t), \tag{18}$$

where the factor of 1/2 is needed because the interaction energy is shared between the molecule and its neighbors and must not be counted twice.

The terminal interaction term should be a significant fraction of the C-C double bond energy. Therefore, we will write $\varepsilon_t = 615f$ kJ, where f is an adjustable parameter. If the molecules are freely rotating, the probability is 1/3 that a neighboring molecule will have the correct orientation to form a bond with a terminal atom. Hence a “nominal” value of f would be 0.33. As we will show below, the value 0.40 gives good agreement with the melting temperature. The other interaction term, ε_p, should be roughly equal to the energy of interaction between planes in graphite, ~4.2 kJ [48], much smaller than the value of ε_t. Using these estimates, together with Equation (18), the binding energy for a C_n molecule is

$${}_B \approx 0.7 + 51.2f/n \text{ MJ/kg.} \tag{19}$$

In this work, we will also treat the density ρ_0 as an adjustable parameter, determined by fitting isobaric expansion data. However, a preliminary estimate can be made as follows. Let each molecule be represented by a rectangular box. Take the box dimensions in the two directions perpendicular to the chain to be approximately equal to the spacing between layers in graphite, 3.37Å, and take the dimension parallel to a chain of n atoms to be 1.28n, where 1.28Å is the typical bond distance. The volume per carbon atom is found to be 14.5Å^3, giving a density 1.4 g/cm^3—the same value for all n.

We have now reduced the calculation of the cold curves for all polyatomic species to two adjustable parameters. We chose $f = 0.40$, to match the melting temperature, and $\rho_0 = 1.0$ g/cm^3, to match the isobaric expansion data. Fixing the value of β_0 as discussed above, we obtain the following cold curve parameters. (The TFD match density was 2 g/cm^3 in all cases.)

SpeciesE_B(MJ/kg)ρ_0(g/cm^3)β_0(GPa)$\Delta H_f^o(298)$(MJ/kg) [16]

$C_2$10.91.024.534.87

C_3 7.51.020.022.76

C_4 5.81.017.320.21

C_5 4.81.015.516.30

Using these parameters, our model gives the following results for the density and Helmholtz free energy of the various carbon species at 0.011 GPa and 4800K, the experimental graphite-liquid-vapor triple point.

Species	A (MJ/kg)	ρ (g/cm^3)
C_1	-15.3	2.87
C_2	-9.1	0.618
C_3	-15.5	0.624
C_4	-12.6	0.631
C_5	-13.3	0.642

All of the polyatomic species have a much lower density than graphite, as required to give the positive slope of the melting line. Since C_3 is the only species having a free energy competitive with that of the monatomic fluid, we would not expect the other species to be important in the liquid state.

Chemical equilibrium calculations, using the PANDA mixture model, give the following results.

- C_3 is the only important polyatomic species in the liquid phase, at temperatures up to ~6000K.
- The concentrations (in weight percent) of C_1 and C_3 are comparable at liquid densities and temperatures near the melting point. The concentration of C_3 increases at lower densities.
- C_2 becomes more important as the temperature increases. The concentrations of C_2 and C_3 are comparable at ~1.0×10^4K. C_2 predominates at higher temperatures.
- C_2 is also important at low temperatures and low densities.
- C_4 and C_5 are unimportant at all densities and temperatures, their concentrations never exceeding ~2% by weight.
- None of the polyatomic species are important at densities above 3 g/cm^3 or temperatures above 5.0×10^4K.

As we will show in Section 5.2, allowing formation of C_3 molecules gives good agreement with the observed melting behavior. At low pressures, the model predicts that the liquid is of a mixture of C_1 and C_3; the liquid density is less than that of graphite, giving a positive slope to the melting curve. At higher pressures, the model predicts the C_1 species to become most important; the liquid density is higher than that of graphite, giving a negative slope to the melting curve. The predicted sublimation pressures also agree fairly well with the experimental data, giving further confirmation of our assumptions.

4. Thermal Electronic Contributions

4.1 General

At sufficiently high temperatures, excitation of electrons out of the ground state configuration makes an important contribution to the thermodynamic properties. In this work, the thermal electronic terms for the metallic phases [subscripted e in Equations. (1)-(3) and (11)] were calculated using the PANDA ionization equilibrium model (IEQ) [18]. The INFERNO model of Liberman [49] was also used to test the IEQ results at high densities.

The IEQ model used in this work includes two improvements to the average atom approximation not discussed in the PANDA manual [18]—corrections for charge fluctuations and for thermal broadening. Therefore, we will give a brief outline of the theory and how it has been modified. (See Reference [18] for additional discussion.)

4.2 Basic Theory

We consider an element with atomic number Z and atomic weight W. A particular configuration of this system is specified by giving the populations of the electronic orbitals, each orbital describing the state of a single electron. To calculate the thermodynamic properties of the system, it is necessary to take a thermal average over all configurations of the system, according to the principles of statistical mechanics.

The PANDA IEQ model uses an average atom approximation to the ionization equilibrium equations. Like other average atom models, the properties of the system are computed by considering the electronic structure of a single atom. However, this model is unique in that it explicitly sums over all electronic configurations of the atom instead of considering a single “average” configuration. The most recent version of the model also includes corrections to the average atom approximation that are discussed below.

The electronic contribution to the Helmholtz free energy is given by

$$A_e = -(RT/W)\ln q_e, \qquad (20)$$

where q_e, the electronic partition function for an “average ion,” is a sum over all Z+1 states of ionization,

$$q_e = \sum_{z=0}^{Z} q_z \exp(-[\delta_z + u_z + z a_f^0(z)]/kT). \qquad (21)$$

Here a_f^0 is the free energy (per electron) for an electron gas in which there are z free electrons per ion. q_z is the partition function and u_z is the ground state energy for an ion of charge z. δ_z is a correction to the average atom model, which is discussed below.

The ion partitition function is given by

$$q_z = \sum_n g_z(n) \exp[-\varepsilon_z(n)/kT] \tag{22}$$

where $g_z(n)$ and $\varepsilon_z(n)$ are the statistical weights and energy levels of the ion, and the sum is taken over all configurations of the electrons. These quantities, along with the ground state energies u_z, are calculated from a scaling model, using a table of orbital radii and energies for the ground state configuration of the isolated atom [50], along with corrections for ionization and continuum lowering, as discussed in Section 9 of Reference [18].

The IEQ model generates a table of the electronic entropy as a function of density and temperature. This table is input to the solid or liquid model. The pressure, internal energy, and Helmholtz free energy are computed from the entropy table, using standard thermodynamic relations. For density-temperature points off the table, PANDA uses the TFD model. See Section 8 of Reference [18] for details.

4.3 Charge Fluctuations

The average atom corrections, δ_z in Equation (21), are new additions to the IEQ model and are not discussed in the PANDA manual. One of the approximations in the average atom model is that charge neutrality holds within an ion sphere. In Reference [51], we showed that there are fluctuations in the charge within an ion sphere, and we derived expressions for the corrections that are valid in the low-density limit. We showed that satisfactory results can be obtained by taking $\delta_z = 0$ for $z>1$. (See Reference [51] for the explicit formulas for δ_0 and δ_1.)

We have not yet found a rigorous theory of charge fluctuations at high densities. However, the fluctuation terms are expected to become less important as the density increases, because of increased attraction between "holes" and "electrons." In order to account for this effect, the low-density values are modified as follows.

$$\delta_z \rightarrow \delta_z \exp(-150 F_3 \rho / W), \tag{23}$$

where F_3 is an input parameter, typically ranging from 0.1 to 1.0. This expression was motivated by a model of electrical conductivity data near the metal-insulator transition [52]. A preliminary comparison with the experimental data indicates that it captures the essential features of the physics.

4.4 Thermal Broadening

Another approximation in the average atom model is that all ion spheres are equal in size. In fact, thermal motions can lead to fluctuations in the sizes of the ion spheres. The latest version ofPANDA includes a correction for this effect.

Consider a configuration of N atoms in which the ion spheres have volumes $v_1, v_2, \ldots, v_N$ that fluctuate about the average volume $\bar{v}$,

$$\bar{v} = N^{-1} \sum_{i=1}^{N} v_i . \tag{24}$$

It follows that

$$\sum_{i=1}^{N} (v_i - \bar{v}) = 0 . \tag{25}$$

The energy of this configuration can be expressed in terms of volume fluctuation by expanding in a Taylor series about the average volume. If $e(v_i)$ is the energy for a single ion sphere of volume v_i,

$$E = \sum_i e(v_i) = Ne(\bar{v}) + \frac{1}{2}\left(\frac{d^2 e}{dv^2}\right)_{\bar{v}} \sum_i (v_i - \bar{v})^2 , \tag{26}$$

where we have discarded terms above second-order. The energy derivative in Eq. (26) can be expressed in terms of the bulk modulus and the sound speed, giving

$$E - \bar{E} \approx kX_B \sum_i (v_i/\bar{v} - 1)^2 \text{, where } X_B = Wc_s^2/2R = 60Wc_s^2 \text{ (Kelvin)}. \tag{27}$$

The statistical-mechanical average of some quantity F over all configurations $v_1, v_2, \ldots, v_N$ is

$$\langle F \rangle = \frac{\int F(v_1 \ldots v_N) \exp[(E - \bar{E})/kT] dv_1 \ldots dv_N}{\int \exp[(E - \bar{E})/kT] dv_1 \ldots dv_N} . \tag{28}$$

To simplify the evaluation of the above integral, we will drop the restriction on the ion sphere volumes, Eq. (25). In that case, the integration over each sphere volume is independent. Then

$$\langle F\rangle \approx \int F(v)\exp[-X_B(v/\bar{v}-1)^2/T]\,dv \Big/ \int \exp[-X_B(v/\bar{v}-1)^2/T]\,dv\,. \tag{29}$$

Equation (29) is the thermal broadening relation that we use to average the IEQ entropy, calculated from the average atom approximation, over fluctuations in density. In practice, the principal effect of this procedure is to smooth discontinuities that arise when bound levels are cut off due to pressure ionization. The smoothing effect is particularly important near the metal-insulator transition, where the ground state of the atom is pressure-ionized.

In the present version of the model, X_B is taken to be a constant and is treated as an input parameter. Smaller values of X_B give more smoothing. Using the ambient sound speed for graphite, a nominal value for carbon is 1.0×10^4 K. However, a much smaller value is appropriate in the metal-insulator transition region, where the sound speed is smaller.

4.5 Application to Carbon

In the present work, the orbital data used in the atomic scaling model were taken from Reference [50], except that the orbital binding energies EA were modified to improve the ionization potentials [53] and the energies of the lowest lying excited states [16] predicted by the model. The revisions were as follows (EA in Hartree):

Orbital	EA (old)	EA (mod)
1S+	-1.1389e+01	-1.1200e+01
2S+	-7.3326e-01	-7.2000e-01
2P-	-3.9904e-01	-4.4000e-01
2P+	-4.4320e-01	-4.2970e-01

The IEQ results were generated using the following parameter settings.

- MX=EFAC=3. MX is the maximum number of electron-hole excitations from the ground state, and EFAC is the energy cutoff, relative to the ionization energy, in the sum over excited states. These factors are large enough to include all important contributions to the ion partition functions.
- F1=F2=1. We chose the default values for these factors, which are used in the continuum-lowering model, because they gave good agreement with the density of the metal-insulator transition obtained using the INFERNO model [49].
- F3=0.1. This constant, used in the average atom corrections, Equation (23), was the same as we have used in calculations for other metals [52].
- XB=1.0×10^{-3}K. This constant, used in the thermal broadening model, Eq. (29), was chosen to get a reasonable amount of smoothing.

The entropy was computed at 63 densities, $1.0\times10^{-10}\le\rho\le1.0\times10^{3}$ g/cc, and at 36 temperatures, $0\le T\le1.16\times10^{8}K$. (The T=0 points were obtained by extrapolation.)

The thermal electronic contributions to the entropy and pressure are shown in Figure 4. The solid curves, calculated from the PANDA IEQ model, show isotherms from 1000 to 1.0×10^8K, equally spaced in the logarithm. The most striking feature of the plots is the insulator-metal transition that occurs in the density range 1-3 g/cm^3. At low densities, the valence electrons are localized, insulating states. The ground state configuration of an isolated carbon atom ($1s^2\ 2s^2\ 2p^2$) has a statistical weight of 15. Hence, the entropy approaches the value $R\ln 15/W = 1.875\times10^{-3}$ MJ/kg/K as $T\to 0$ at low densities. At high densities, the valence electrons are pressure-ionized, becoming delocalized, metallic states. The entropy approaches zero as $T\to 0$ at high densities. This insulator-metal transition results in the dramatic drop in entropy that is seen in the range 1-3 g/cm^3. The same phenomenon causes a large thermal electronic contribution to the pressure in this density range.

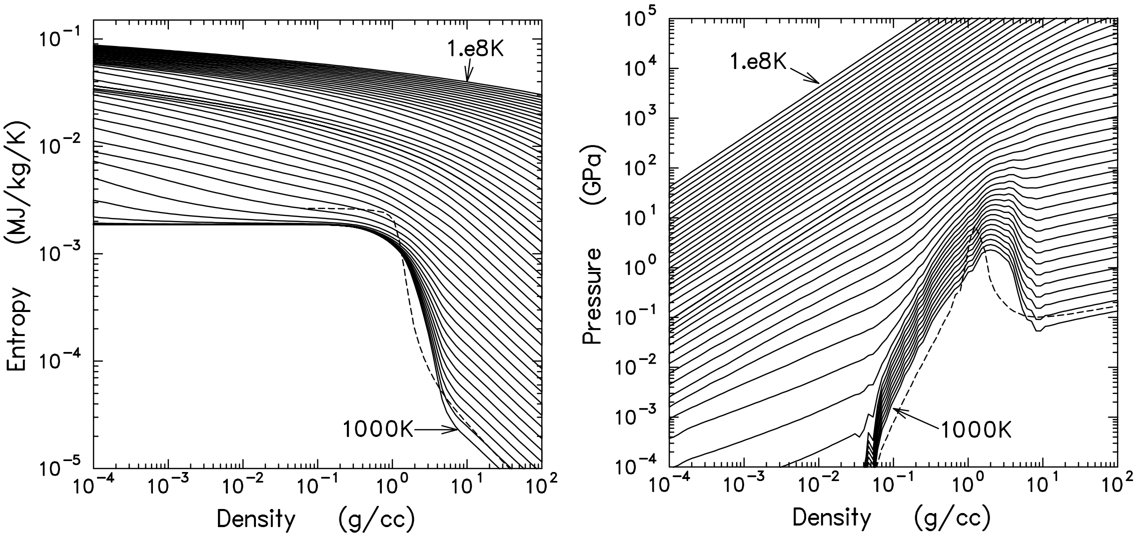

Figure 4. Thermal electronic contributions to entropy and pressure for metallic carbon. Solid curves, calculated from the PANDA IEQ model, show 47 isotherms from 1000 to 1.0x10^8K, equally spaced in the logarithm. Dashed curves are 1000K isotherms computed using the INFERNO model.

Because the IEQ model uses a relatively simple treatment of continuum lowering and pressure ionization, there is some question as to the accuracy of its predictions in the insulator-metal transition region. For comparison, the 1000K isotherm computed from the INFERNO model is shown by a dashed line in Figure 4. INFERNO is a sophisticated numerical model that solves the Dirac equation for the energy levels and treats both bound and free states in a consistent manner [49]. Previous work showed that INFERNO gives very good predictions of the effect of the insulator-metal transition on the shock Hugoniot of xenon, in which the transition is induced under pressure [46][54]. The fact that the INFERNO and IEQ results predict a insulator-metal transition in the same density range gives further support to our model.

However, there are two differences between INFERNO and IEQ that should be noted. First, INFERNO gives a higher entropy than IEQ at low densities. The INFERNO result is incorrect at low densities because of an error introduced by the average configuration approximation, as explained in Reference [51]. Second, INFERNO predicts a sharper drop in entropy at the transition because it does not include any thermal broadening. For these reasons, we consider IEQ to be the more accurate model for carbon, even though it uses a more simplified treatment of continuum lowering and pressure ionization.

Finally, we note that the above results support our assumption that liquid carbon is metallic at densities above about 3 g/cm^3. At lower densities, the transition seen in the electronic structure, along with the formation of molecular species in the liquid state, could be responsible for the observed drop in thermal conductivity [14].

5. Results and Discussion

5.1 Multiphase EOS Calculations

The PANDA MOD MIX option was used to construct a single EOS table for a fluid phase mixture of C_1, C_2, and C_3. (C_4 and C_5 were not included in the final EOS because they were found to be unimportant, as discussed in Section 3.4.) In order to eliminate numerical problems in the mixture model, it was necessary to include Maxwell constructions in the EOS tables for the various species.

Next, the PANDA MOD TRN option was used to compute the phase diagram and construct the multiphase EOS, including four phases—graphite, diamond, metallic solid, and the fluid mixture. The “imperfect” form of diamond was used in making the EOS table, in order to match the shock data as discussed below.

The mesh used in making the multiphase EOS table included 84 densities in the range $1.0 \times 10^{-10} \le \rho \le 100$, plus a $\rho = 0$ point, and 74 temperatures in the range $0 \le T \le 1.0 \times 10^{8}$. The mesh points were chosen to give good resolution of the phase transitions and other important features of the EOS surface. In order to allow treatment of fracture models, a tension region was included at temperatures below the sublimation point (TSPALL=3600). Maxwell constructions were included at all higher temperatures, as noted above.

The new EOS table has been added to the SNL-SESAME library (file “sesame”) as material number 7830.

5.2 Equilibrium Phase Diagram

Our calculated phase diagram is shown in Figure 5, along with some of the experimental data. The data, which are quite limited, are summarized as follows.

- Kennedy and Kennedy measured the graphite-diamond boundary from 1273 K to 1900 K [55]; their data are shown by crosses in Figure 5. Bundy’s estimate of the phase line [1], shown by a dotted line, is based on experimental data from 1250 to 2900K.
- Measurements of the graphite-melting curve have been made by Bundy [56], Fateeva and Vereschchagin [57], and Togaya, et al. [15]. All three sets of experiments show a peak in the melting temperature near 5-6 GPa. The data of Togaya, et al. are the most recent and are thought to be most accurate [4]; they are shown by x’s in Figure 5.
- Musella, et al. have recently reported very careful and accurate measurements of the melting behavior near the triple point [14]. They also give an incisive discussion of other experiments. Their melting temperature is 150K higher than that of Togaya, et al., who did not measure the temperature directly. The squares

in Figure 5 show the point of Musella, et al., together with the data of Togaya, et al., shifted by +150K.

- The diamond melting line has not been measured directly. However, it is currently thought that the phase boundary has a positive slope, based on sound speed measurements of Shaner, et al. [58][59]. We will discuss those experiments in Section 5.5.

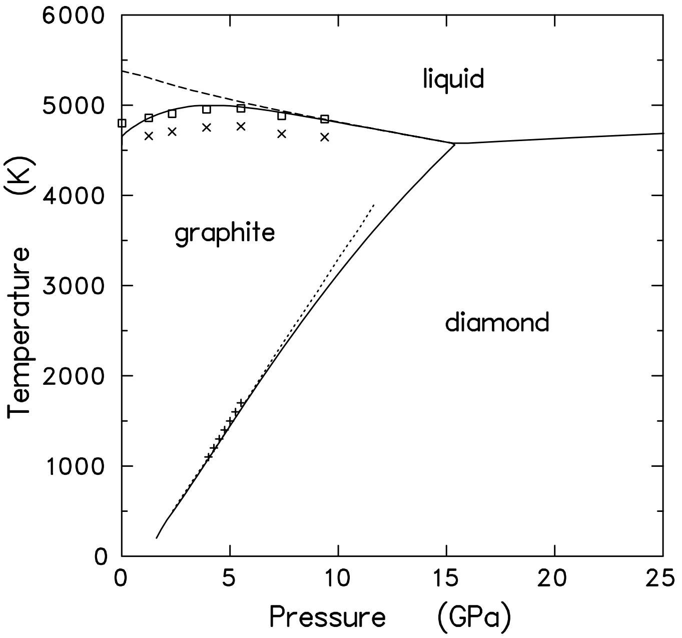

Figure 5. Phase diagram for carbon. Experimental data: crosses [55]; dotted curve [1] (extrapolation above 2900K); x's [15]; squares [14], and data of [15], shifted by +150K. The solid curves are our calculated boundaries. The dashed curve is the calculated melting curve when molecular species are excluded from the liquid phase.

As seen in Figure 5, our calculated phase diagram agrees quite well with the existing data. Our graphite-diamond boundary deviates slightly from Bundy's extrapolation [1] at high temperatures. The reason is that his extrapolation assumes a constant difference in heat capacity between graphite and diamond. Our model, which uses a more sophisticated treatment of the lattice vibrational terms, does not make that assumption.

Our calculated melting curve shows the observed behavior—a positive slope at low pressures, a maximum near 5 GPa, and a negative slope at high pressures. As noted in Section 3.3, one of the parameters in the liquid model (EFAC) was adjusted to match the high-pressure behavior. We chose to match the data of Togaya, et al., shifted by +150K. The calculated phase line is within the uncertainties in the experimental data.

The formation of polyatomic molecules, especially C_3, plays an essential role in matching the distinctive character of the graphite-melting curve. The dashed line in Figure 5 shows the melting curve obtained when only the monatomic species C_1 is allowed to form. In that case, the melting curve has a negative slope at all pressures up to the graphite-diamond-liquid triple point. Formation of the polyatomic molecules lowers the density of the liquid phase and gives a positive slope at low pressures, in agreement with the observed behavior.

Our model predicts a graphite-liquid-vapor triple point at 0.017 GPa and 4660K, close to the recent measurements of Musella, et al. (0.011±0.002 GPa and 4800±150K [14]). Our sublimation point is 3800K, in satisfactory agreement with other work [16][60].

5.3 Melting Data

Because it is very difficult to perform experiments on liquid carbon [14], there are no precise measurements of the enthalpy and density changes at the melting point. Baitin, et al., estimated the enthalpy of fusion to be 10.4 MJ/kg, using the exploding wire technique [61]. Musella, et al., estimated a 45% volume change on melting, based upon the void volume obtained in recovered melted samples [14].

The isobaric expansion experiments of Gathers, et al. [62], also provide some information about the melting behavior. Glassy carbon samples, kept at constant pressure by a neutral gas, were resistively heated. The current-voltage data were used to determine the enthalpy as a function of time. The density was determined as a function of time from streak camera measurements of the sample diameter.

Figure 6 shows the measured enthalpy vs. density for samples at 0.2 and 0.4 GPa. The samples had an initial density of 1.83 g/cm^3. On heating, the samples first expand slightly, then contract to near the theoretical density at an enthalpy of 7 MJ/kg, which corresponds to a temperature near 4000K, below the melting point.

Our calculations of the isobaric experiments are compared with the data in Figure 6. (Since the calculations were made for nonporous graphite, only the results above 7 MJ/kg should be compared with the data.) According to our model, melting occurs at an enthalpy of about 9 MJ/kg. There is a sharp change in slope as the samples enter the mixed phase region, shown by dotted lines. Melting is complete at about 21 MJ/kg, which corresponds to the upper end of the measurements. The calculated enthalpy of fusion is 12 MJ/kg. The calculated density change is 50%.

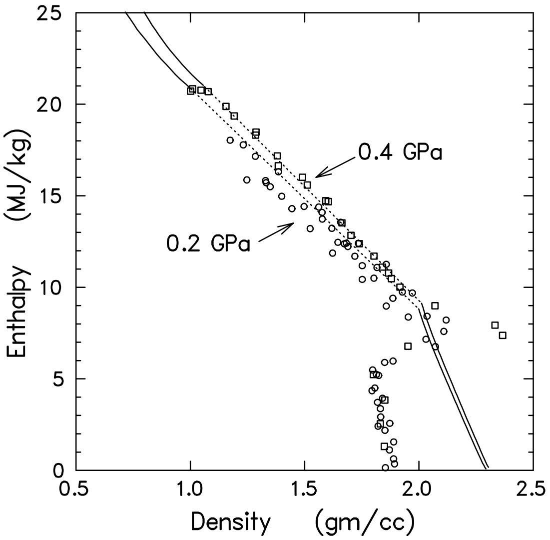

Figure 6. Isobaric expansion data for carbon. Experimental data: circles—0.2 GPa, squares—0.4 GPa. Curves are calculated from our model, the dotted portions showing the mixed phase region.

It should be noted that the ρ_0 parameter in the model for the polyatomic species (Section 3.4) was chosen to agree with these isobaric data. It may be that forcing such good agreement is not justified by the errors and uncertainties in the experimental technique. However, the choice we have made is reasonably consistent with the data available at the present time.

5.4 Nonequilibrium Behavior

As we have already observed, the transition from graphite to diamond does not occur at the equilibrium pressure under shock loading conditions. Many aspects of this nonequilibrium behavior can be described by treating diamond as an imperfect crystal. Our model (Section 2.4) treats this imperfect form of diamond as a crystal containing vacant sites. Because the energy required to create a vacancy is large, compared with the free energy difference between graphite and diamond, creation of 3% vacant sites shifts the transition pressure by an order of magnitude.

Figure 7 compares the equilibrium and nonequilibrium phase diagrams. In the equilibrium case, shown by solid curves, the transition from diamond to the metallic solid occurs at a pressure of 900 GPa at zero temperature. Because the metallic solid is denser than diamond (see Figure 1), the phase line has a negative slope, terminating at the melting curve. The diamond-metal-liquid triple point occurs at 220 GPa and 5400K.

The dashed lines in Figure 7 show how the phase boundaries shift when diamond is replaced by its imperfect form. The diamond field of stability is substantially reduced. The graphite-diamond transition pressure is increased, while the diamond-metal transition pressure drops significantly. In addition, the metallic solid becomes more stable than diamond at high temperatures, so that diamond does not intersect the melting curve at any pressure. (This possibility was considered by Grover in his sensitivity studies of the carbon phase diagram [63].)

As we will show below, this nonequilibrium phase diagram is consistent with the available shock wave data for carbon.

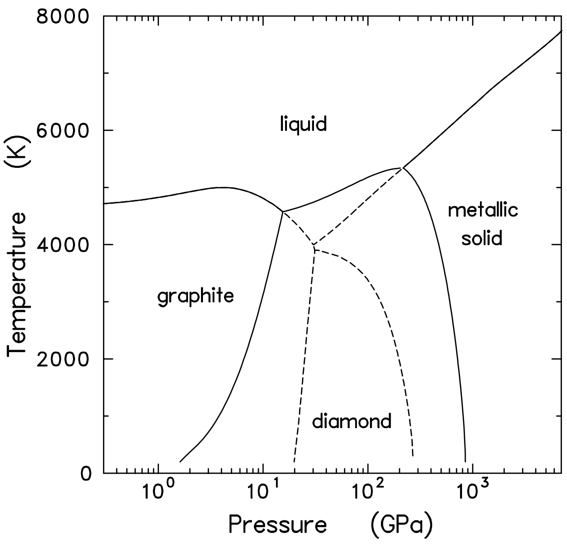

Figure 7. Comparison of phase diagrams for carbon. Solid curves—equilibrium phase lines. Dashed curves—phase lines obtained with an “imperfect” diamond phase containing 3% vacancies.

5.5 Shock-Wave Behavior

Figure 8 shows the nonequilibrium phase diagram, together with pressure-temperature Hugoniot loci for several initial densities in the range 0.12 to 2.16 g/cm^3. It can be seen that shock wave measurements for these initial densities sample the phase diagram over a wide range of temperatures and pressures. The higher-density materials are shocked into the diamond and metallic solid phases, the transition pressures dependent upon the initial density. The lower-density materials traverse only the graphite and liquid phases.

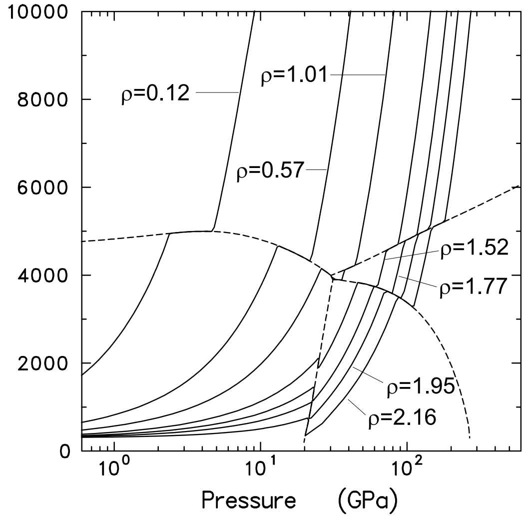

Figure 8. Shock-induced phase transitions in carbon. Solid lines are Hugoniot curves for various initial densities, as indicated. Dashed lines are calculated (non-equilibrium) phase boundaries.

Figures 9 and 10 compare our calculated Hugoniots with experimental data [26][27][64] in the shock velocity-particle velocity plane. The agreement is very good. At the four highest densities, the graphite-diamond transition is the most dramatic feature of the Hugoniot. However, the calculated Hugoniot for ρ = 2.16 also exhibit a change in slope, for u_p in the range 4-5 km/s, due to the transition between diamond and the metallic solid. This feature is also seen in the data, as observed by Gust when reporting his data for Ceylon graphite [27].

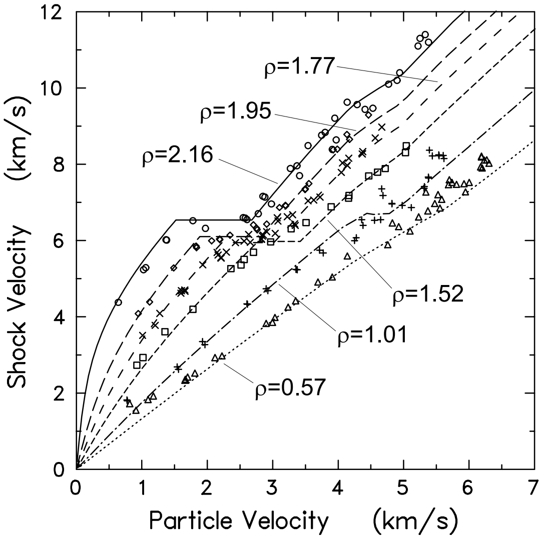

Figure 9. Hugoniots for carbon at various initial densities. Curves are calculated. Discrete points are data from Refs.[26][27].

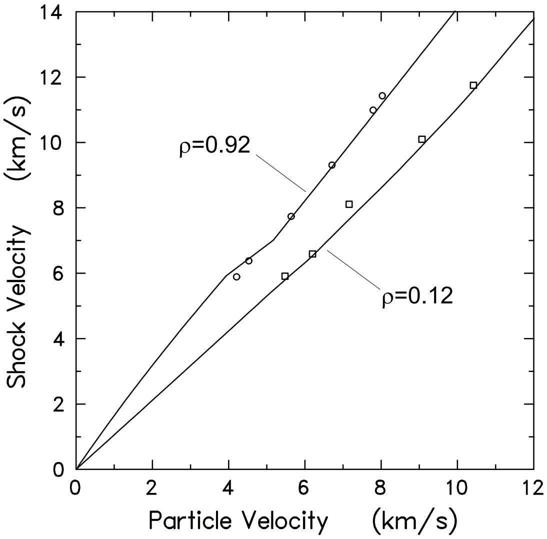

Figure 10. Hugoniot data for carbon aerogel foams. Curves are calculated. Discrete points are from Reference [64].

As expected from Figure 8, the lower-density carbon Hugoniots does not exhibit the graphite-diamond phase transition. However, they do exhibit changes in slope that are due to the melting of graphite. This feature is especially evident in the data for $\rho = 1.01$ for u_P in the range 4-5 km/s.

Figure 10 shows Hugoniot data for special low-density carbon foams called “aerogels” [64]. These data also extend to higher velocities than those in Figure 9. Except for the two lowest pressure points for $\rho = 0.92$, all of these data lie in the fluid region. The shock temperatures are also quite high, up to 1.5×10^4K at the highest pressures, where thermal electronic excitations make the most important contribution to the EOS. Our model gives very good results for these aerogel foams, just as it does for other types of carbon.

Shaner, et al. have investigated the sound speed in shocked graphite ($\rho = 2.20$) by measuring the rarefaction wave velocities at shock pressures between 80 and 140 GPa [58]. Their data are compared with our calculations in Figure 11. The measured velocities are roughly 20% higher than the bulk sound speeds, indicating the presence of material strength. Based on these results, they concluded that shock melting does not occur below 140 GPa, which they took as a lower bound to the diamond-melting boundary.

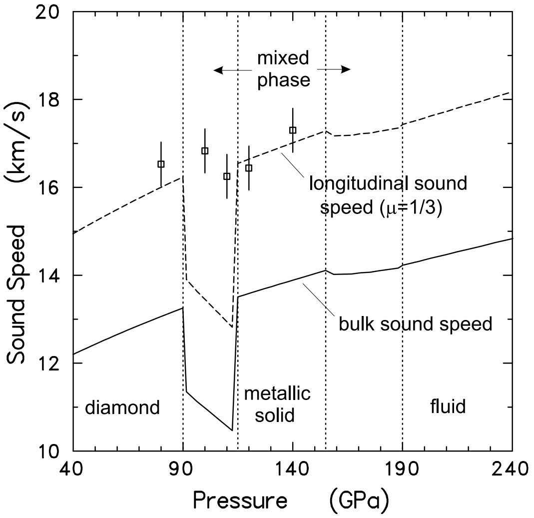

Figure 11. Sound speed for shock-compressed graphite. Circles, with error bars, are from Reference [58]. Theoretical curves: solid—bulk sound speed; dashed—longitudinal sound speed computed using Poisson’s ratio of 1/3. Dotted vertical lines show boundaries of mixed phase regions.

Our bulk sound speed is shown by the solid curve in Figure 11. The longitudinal sound speed, estimated from the bulk sound speed using a Poisson’s ratio of 1/3, is in good agreement with the data. Our model predicts that melting does not begin until a shock pressure of 155 GPa, in agreement with the conclusions of Reference [58]. However, we also predict a transition from diamond to the metallic phase in the pressure range 90-115 GPa. As seen in Figure 11, the data show a discontinuity in this vicinity; this feature could be due to the diamond-metal transition, but the error bars are too large to make a definite statement to that effect.

Mitchell, et al., measured the electrical conductivity of shocked pyrolytic graphite [59]. These experiments confirmed the existence of a transition from the conducting graphite phase to the insulating diamond phase. No metallic conductivity was observed up to the highest shock pressure, 63 GPa. However, this pressure is considerably lower than our prediction of the metallic transition.

5.6 Shock Vaporization

Wise, et al., used the shock-vaporization technique to study the expansion behavior of shocked carbon at low pressures [65]. Porous carbon samples ($\rho = 1.4$) were shocked to 100 GPa and 8000K, then allowed to expand across a gap and impact a target plate. The release temperature was about 4000K. A VISAR was used to record the motion of the target as a function of time. Two experiments were performed—one with a 5-mm gap, the other with a 10-mm gap. Numerical simulations of these experiments, using an earlier EOS model for liquid carbon, did not give satisfactory agreement with the data.

We have made numerical simulations of these experiments using the CTH hydrocode. The results are compared with the experimental data in Figure 12. Zero time corresponds to arrival of the shock wave at the surface of the carbon sample and is absolute in both the experiment and calculations; no adjustment was made to match the results.

The simulations were made with two liquid models that did not allow refreezing on release. The dotted curves are simulations in which the liquid consists only of the monatomic species. As in Reference [65], the time of arrival is late, and the peak velocity is much too high. The solid lines are simulations using the fluid mixture model, which includes formation of the polyatomic molecules. Here the time of arrival and shape of the first peak are in very good agreement with the data. There are still discrepancies with the data at later times, some of which could be due to two-dimensional effects.

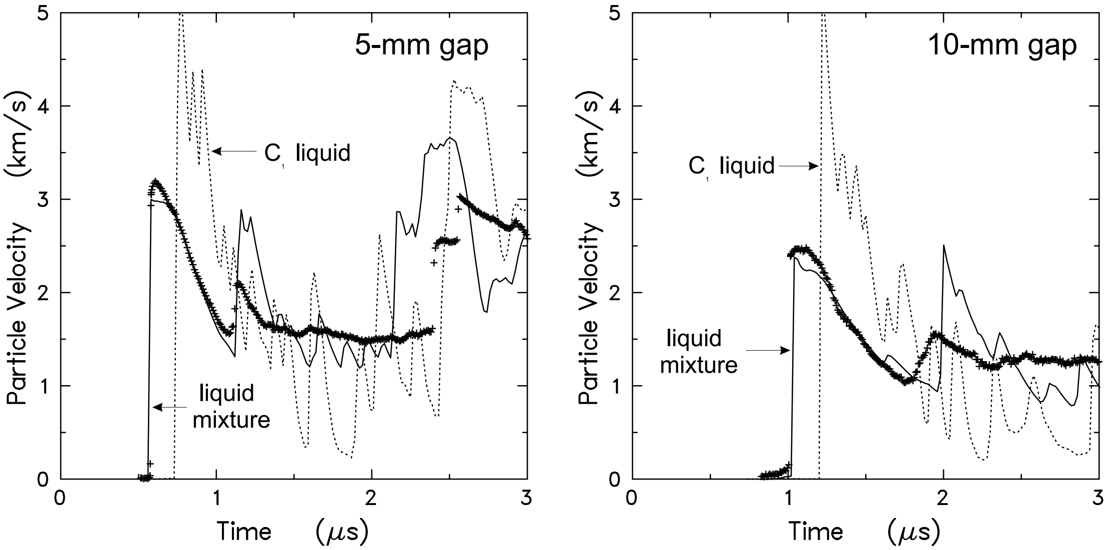

Figure 12. Shock vaporization experiments on carbon. Crosses are experimental data from Reference [65]. Solid curves are CTH calculations using EOS for liquid mixture. Dotted curves are calculations assuming liquid consists only of monatomic species.

6. Conclusions and Recommendations

We have developed a new tabular equation of state for carbon, which includes treatment of solid-solid phase transitions, melting, vaporization, chemical reactions, and thermal electronic excitation. The EOS is in good agreement with experimental thermophysical data, static compression data, phase boundaries, and shock-wave measurements.

The new EOS table has been added to the SNL-SESAME library as material number 7830 and is available for use in calculations using CTH and other hydrocodes. This EOS covers such a wide range of densities (0 - 100 g/cm^3) and temperatures (0 - 1.0×10^8K) that it should be suitable for virtually any standard hydrocode problem. It is applicable to porous carbon materials, including aerogels, as well as denser forms.

The new EOS will also play an important role in developing improved EOS tables for a variety of other materials containing carbon—explosive detonation products, the reaction products of plastics, polymers, and organic substances, and carbon composites.

We believe that this new EOS is a significant improvement in the modeling of carbon and materials containing carbon. However, there are still many issues that deserve additional investigation. In particular, new experimental data on the melting behavior and properties of the liquid would be useful to improve the calibration of certain model parameters. Additional experimental and theoretical work on the properties of polyatomic carbon molecules in the liquid phase would be desirable. Finally, development of a time-dependent model of the graphite-diamond transition and other nonequilibrium behavior would be a noteworthy achievement.

References

[1] F. P. Bundy, ‘‘The P,T Phase and Reaction Diagram for Elemental Carbon, 1979,’’ J. Geophys. Res. **85**, 6930-6936 (1980).

[2] P. Gustafson, “An Evaluation of the Thermodynamic Properties and the P,T Phase Diagram of Carbon,” Carbon **24**, 169-176 (1986).

[3] F. P. Bundy, ‘‘Pressure-Temperature Phase Diagram for Elemental Carbon,’’ Physica **A 156**, 169-178 (1989).

[4] F. P. Bundy, W. A. Bassett, M. S. Weathers, R. J. Hemley, H. K. Mao, and A. F. Goncharov, “The Pressure-Temperature Phase and Transformation Diagram for Carbon; Updated Through 1994,” Carbon **34**, 141-153 (1996).

[5] L. Pauling, *The Nature of the Chemical Bond* (Cornell University Press, Ithaca, N. Y., 1960) 3rd. Ed.

[6] O. L. Blakslee, D. G. Proctor, E. J. Seldin, G. B. Spence, and T. Weng, ‘‘Elastic Constants of Compression-Annealed Pyrolytic Graphite,’’ J. Appl. Phys. **41**, 3373-3389 (1970).

[7] W Krätschmer, L. D. Lamb, K. Fostiropoulos, and D. R. Huffman, “Solid C_{60}: A New Form of Carbon,” Nature **347**, 354-358 (1990).

[8] B. E. Warren, “X-Ray Diffraction in Random Layer Lattices,” Phys. Rev. **59**, 693-698 (1941).

[9] J. Robertson, ‘‘Amorphous Carbon,’’ Adv. Phys. **35**, 317-374 (1987).

[10] S. K. Das and E. E. Hucke, ‘‘Experimental Measurements on Configurational Free Energy Change of the Graphite-Glassy Carbon Equilibrium,’’ Carbon **13**, 33-41 (1975).

[11] G. I. Kerley, ‘‘Theoretical Equations of State for the Detonation Properties of Explosives," in Proceedings of the Eighth Symposium (International) on Detonation, edited by J. M. Short, NSWL MP 86-194 (Naval Surface Weapons Center, White Oak, MD, 1986), pp. 540-547.

[12] G. I. Kerley, ‘‘Theoretical Model of Explosive Detonation Products: Tests and Sensitivity Studies," in Proceedings of the Ninth Symposium (International) on Detonation, edited by W. J. Morat, OCNR 113291-7 (Office of the Chief of Naval Research, 1990), pp. 443-451.

[13] G. I. Kerley and T. L. Christian-Frear, “Prediction of Explosive Cylinder Tests Using Equations of State from the PANDA Code,” Sandia National Laboratories report SAND93-2131, 1993.

[14] M. Musella, C. Ronchi, M. Brykin, and M. Sheindlin, “The Molten State of Graphite: An Experimental Study,” J. Appl. Phys. **84**, 2530-2537 (1998).

[15] M. Togaya, S. Sugiyama, and E. Mizuhara, “Melting Line of Graphite,” in High Pressure Science and Technology - 1993, edited by S. C. Schmidt, J. W; Shaner, G. A. Samara, and M. Ross (AIP Conference Proceedings 309, 1994) pp. 255-258.

[16] M. W. Chase, Jr., C. A. Davies, J. R. Downey, Jr., D. J. Frurip, R. A. McDonald, and A. N. Syverud, “JANAF Thermochemical Tables,” J. Phys. Chem. Reference Data **14**, Supp. No. 1 (1985).

[17] K. S. Pitzer and E. Clementi, ‘‘Large Molecules in Carbon Vapor,’’ J. Am. Chem. Soc. **81**, 4479-4485 (1959).

[18] G. I. Kerley, “User’s Manual for PANDA II: A Computer Code for Calculating Equations of State,” Sandia National Laboratories report SAND88-2291, 1991.

[19] J. M. McGlaun, F. J. Ziegler, S. L. Thompson, L. N. Kmetyk, and M. G. Elrick, “CTH - User's Manual and Input Instructions,” Sandia National Laboratories report SAND88-0523, April 1988.

[20] J. M. McGlaun, S. L. Thompson, and M. G. Elrick, “CTH: A Three-Dimensional Shock Wave Physics Code,” Int. J. Impact Engng. 10, 351-360 (1990).

[21] J. M. McGlaun, S. L. Thompson, L. N. Kmetyk, and M. G. Elrick, “A Brief Description of the Three-Dimensional Shock Wave Physics Code CTH,” Sandia National Laboratories report SAND89-0607, July 1990.

[22] E. S. Hertel, Jr. and G. I. Kerley, “CTH EOS Package: Introductory Tutorial,” Sandia National Laboratories report SAND98-0945, 1998.

[23] E. S. Hertel, Jr. and G. I. Kerley, “CTH Reference Manual: The Equation of State Package,” Sandia National Laboratories report SAND98-0947, 1998.

[24] B. K. Godwal, S. K. Sikka, and R. Chidambaram, “Equation of State Theories of Condensed Matter Up To About 10 TPa,” Phys. Rep. **102**, 121-197 (1983).

[25] M. Hanfland, H. Beister, and K. Syassen, ‘‘Graphite Under Pressure: Equation-of-State and First-Order Raman Modes,’’ Phys. Rev. B **39**, 12598-12603 (1989).

[26] S. P. Marsh, *LASL Shock Hugoniot Data* (University of California Press, Berkeley, 1980).

[27] W. H. Gust, ‘‘Phase Transition and Shock-Compression Parameters to 120 GPa for Three Types of Graphite and for Amorphous Carbon,’’ Phys. Rev. B **22**, 4744-4756 (l980).

[28] D. J. Erskine and W. J. Nellis, “Shock-Induced Martensitic Transformation of Oriented Graphite to Diamond,” Nature, Vol.**349**, 317-319 (1991).

[29] D. J. Erskine and W. J. Nellis, “Shock-Induced Martensitic Transformation of Highly Oriented Graphite to Diamond,” J. Appl. Phys.**71**, 4882-4886 (1992).

[30] I. V. Aleksandrov, A. F. Goncharov, A. N. Zisman, and S. M. Stishov, ‘‘Diamond at High Pressures: Raman Scattering of Light, Equation of State, and High-Pressure Scale,’’ Sov. Phys. JETP **66**, 384-390 (1988).

[31] R. Al-Jishi and G. Dresselhaus, “Lattic-Dynamical Model for Graphite,” Phys. Rev. B **26**, 4514-4522 (1982).

[32] Y. S. Touloukian, R. K. Kirby, R. E. Taylor, and T. Y. R. Lee, ‘‘Thermal Expansion, Nonmetallic Solids,’’ Thermophysical Properties of Matter (IFI/Plenum, New York, 1977) Vol. 13.

[33] R. Hultgren, P. D. Desai, D. T. Hawkins, M. Gleiser, K. K. Kelley, and D. D. Wagman, *Selected Values of the Thermodynamic Properties of the Elements* (American Society for Metals, Metals Park, Ohio, 1972).

[34] S. Fahy and S. G. Louie, ‘‘High-Pressure Structural and Electronic Properties of Carbon,’’ Phys. Rev. B **36**, 3373-3385 (1987).

[35] J. F. Cannon, “Behavior of the Elements at High Pressures,” J. Phys. Chem. Reference Data **3**, 781-824 (1974).

[36] H. J. McSkimin and P. Andreatch, Jr., “Elastic Moduli of Diamond as a Function of Pressure and Temperature,” J. Appl. Phys. **43**, 2944-2948 (1972).

[37] See, for example, C. Kittel, *Introduction to Solid State Physics* (Wiley, New York, 1963), 2nd Ed., pp 122-125.

[38] M. Hanfland, K. Syassen, S. Fahy, S. G. Louie, and M. L. Cohen, ‘‘Pressure Dependence of the First-Order Raman Mode in Diamond,’’ Phys. Rev. B **31**, 6896-6899 (1985).

[39] Handbook of Chemistry and Physics, edited by David R. Lide (CRC Press, Boca Raton, 1996) 77th edition.

[40] M. T. Yin and M. L. Cohen, “Will Diamond Transform under Megabar Pressures?” Phys. Rev. Lett. **50**, 2006 (1983).

[41] R. Biswas, R. M. Martin, R. J. Needs, and O. H. Nielsen, “Complex Tetrahedral Structures of Silicon and Carbon under Pressure,” Phys. Rev. B **30**, 3210-3213 (1984).

[42] A. Y. Liu, M. L. Cohen, K. C. Hass, and M. A. Tamor, “Structural Properties of a Three-Dimensional All-sp2 Phase of Carbon,” Phys. Rev. B **43**, 6742-6745 (1991).

[43] A. Y. Liu and M. L. Cohen, “Theoretical Study of a Hypothetical Metallic Phase of Carbon,” Phys. Rev. B **45**, 4579-4581 (1992).

[44] G. I. Kerley, “Multiphase Equation of State for Iron,” Sandia National Laboratories report SAND93-0027, 1993.

[45] G. I. Kerley, “Perturbation Theory and the Thermodynamic Properties of Fluids II. The CRIS Model,” J. Chem. Phys. **73**, 478-486 (1980).

[46] G. I. Kerley, “A Model for the Calculation of Thermodynamic Properties of a Fluid Using Hard-Sphere Perturbation Theory and the Zero-Kelvin Isotherm of the Solid," in Molecular Based Study of Fluids, edited by J. M. Haile and G. A. Mansoori (Am. Chem. Soc., Washington, DC., 1983) pp. 107-138.

[47] J. H. Rose, J. R. Smith, F. Guinea, and J. Ferrante, “Universal Features of the Equation of State of Metals,” Phys. Rev. B **29**, 2963-2969 (1984).

[48] L. A. Girifalco and R. A. Lad, “Energy of Cohesion, Compressibility, and the Potential Energy Functions of the Graphite System,” J. Chem. Phys. 25, 693-697 (1956).

[49] D. A. Liberman, “Self-Consistent Field Model for Condensed Matter,” Phys. Rev. B **20**, 4981-4989 (1979).

[50] G. I. Kerley, “Atomic Orbital Data for Elements with Atomic Numbers $1 \leq Z \leq 103$,” Sandia National Laboratories report SAND88-2594, 1988.

[51] G. I. Kerley, “Theory of Ionization Equilibrium: An Approximation for the Single Element Case,” J. Chem. Phys. **85**, 5228-5231 (1986).

[52] G. I. Kerley, “Modification of the Lee-More Conductivity Model: Improved Calculation of Ionization State,” Kerley Publishing Services report KPS99-2, Albuquerque, NM, February 1999.

[53] R. D. Cowan, *The Theory of Atomic Structure and Spectra* (University of California, Berkeley, 1981) pp. 12-15.

[54] G. I. Kerley, “Theoretical Model of Liquid Metals,” in Proceedings of the Eighth Symposium on Thermophysical Properties, J. V. Sengers (Ed.) (Am. Soc. Mech. Engineers, New York, NY, 1982) Vol II, pp. 159-164.

[55] C. S. Kennedy and G. C. Kennedy, “The Equilibrium Boundary Between Graphite and Diamond,” J. Geophys. Res. **81**, 2467-2470 (1976).

[56] F. P. Bundy, “Melting of Graphite at Very High Pressure,” J. Chem. Phys. **38**, 618-630 (1963).

[57] N. S. Fateeva and L. F. Vereshchagin, “Concerning the Melting Point of Graphite up to 90 kbar,” JETP Lett. **13**, 110-111 (1971).

[58] J. W. Shaner, J. M. Brown, C. A. Swenson, and R. G. McQueen, “Sound Velocity of Carbon at High Pressures,” J. de Physique **45**, C8235-237 (1984).

[59] A. C. Mitchell, J. W. Shaner, and R. N. Keeler, “The Use of Electrical Conductivity Experiments to Study the Phase Diagram of Carbon,” Physica **139**, 386-389 (1986).

[60] H. B. Palmer, “On the Equilibrium Vapor Pressure of Graphite and the Temperature of the Carbon Arc,” Carbon **8**, 243-244 (1970).

[61] A. V. Baitin, A. A. Levedev, S. V. Romanenko, V. N. Senchenko, and M. A. Schendlin, “The Melting Point and Optical Properties of Solid and Liquid Carbon at Pressures of Up to 2 kbar,” High Temp. - High Pres. **21**, 157-170 (1990).

[62] G. R. Gathers, J. W. Shaner, and D. W. Young, “High-Temperature Carbon Equation of State,” Lawrence Livermore Laboratory report UCRL-51644, September 14, 1974.

[63] R. Grover, “Does Diamond Melt?,” J. Chem. Phys. **71**, 3824-3829 (1979).

[64] N. C. Holmes, “Shock Compression of Low-Density Foams,” in High Pressure Science and Technology - 1993, edited by S. C. Schmidt, J. W; Shaner, G. A. Samara, and M. Ross (AIP Conference Proceedings 309, 1994) pp. 153-156.

[65] J. L. Wise, G. I. Kerley, and T. G. Trucano, ‘‘Shock-Vaporization Studies on Zinc and Porous Carbon," in Shock Waves in Condensed Matter - 1991, edited by S. C. Schmidt, R. D. Dick, J. W. Forbes, and D. G. Tasker (Elsevier, 1992) pp. 61-64.

Distribution

1 General Dynamics Electric Boat Division
Attn: Chris Abate, MS D5-4
7500 Eastern Point Road
Groton, CT 06340-4989

1 New Mexico Tech
Attn: Robert Abernathy, EMRTC
Socorro, NM 87801

1 USAE Waterways Experiment Station
Attn: Mark D.Adley
3909 Halls Ferry Road
Vicksburg, MI 39180-6199

1 California Institute of Technology
Seismological Laboratory 252-21
Attn: Thomas J.Ahrens
Pasadena, CA 91125

1 Southwest Research Institute
Attn: Charles E.Anderson
P. O. Drawer 28510
San Antonio, TX 78228-0510

4 Applied Research Associates, Inc
Attn: D. E. Grady
B. L. Bingham
C. Scheffield
4300 San Mateo Blvd. NE, Suite A-220
Albuquerque, NM 87110

4 Applied Research Associates
Attn: P. T. Dzwilewski
K. Edquist
L. Brown
G. Recht
5941 South Middlefield Rd., Suite 100
Littleton, CO 80123

1 Kaman Sciences Corporation
Attn: Nasit Ari
P. O. Box 7463
Colorado Springs, CO 80933

1 USAE Waterways Experiment Station
Attn: Byron J. Armstrong
3909 Halls Ferry Rd
Vicksburg, MS 39180

1 U. S. Army ARDEC
SMCAR-AEE-WW
Attn: Ernest L. Baker
Picatinny Arsenal, NJ 07806-5000

1 Institute for Defense Analyses
Attn: Bohdan Balko
1801 North Beauregard Street
Alexandria, VA 22311

1 Lockheed Martin Launching Systems
VLS Loading Dock
Attn: Larry Barisciano
103 Chesapeake Park Plaza
Baltimore, MD 21220-0931

1 Applied Physics Lab
Attn: Olivier Barnouin-Jha
John Hopkins Road
Laurel, MD 20723-6099

1 USAE Waterways Experiment Station
Attn: Tommy Bevins
3909 Halls Ferry Rd
Vicksburg, MS 39180

1 Commander: U.S. Army TACOM
AMSTA-TR-R MS 263
Attn: Krishan D. Bishnoi
Warren, MI 48397-5000

1 The University of Texas at Austin
Institute for Advanced Technology
Attn: Stephan J. Bless
4030-2 W. Braker Lane, Suite 200
Austin, TX 78712

1 Wright Laboratory
WL/MNSA
Attn: Dan Brubaker
Eglin AFB, FL 32542-5434

1 Hughes Missile Systems Co.
Attn: David Campbell
Bldg 805 MS C4
PO Box 11337
Tucson AZ, 85734

1 Teledyne Brown Engineering
Attn: Burton S. Chambers III
M/S 66
PO Box 070007
Huntsville, AL 35807-7007

1 Aerojet Propulsion Division
Attn: Bounmy Chhouk
Department 5215
P.O. Box 13222
Sacramento, CA 95813-6000

1 U. S. Army ARDEC
SMCAR-AEE-WW - Bldg. 3022
Attn: Chuck Chin
Picatinny Arsenal, NJ 07806-5000

1 NASA Johnson Space Center
Attn: Eric L. Christiansen
Mail Code SN3
Houston, TX 77058

1 Lockheed Martin Idaho Tech - INEL
Attn: Henry Chu
M/S 0206
P.O. Box 1625
Idaho Falls, ID 83415-0206

1 Thiokol Corporation
Science & Engineering Division
Attn: Dwight Clark
Mailstop 280
P. O. Box 707
Brigham City, Utah 84302-0707

1 MEVATEC
Attn: Steve Clark
1525 Perimeter Parkway, Suite 500
Huntsville, AL 35806

1 DynaEast Corporation
Attn: William Clark
3620 Horizon Drive
King of Prussia, PA 19104

1 Talley Defense Systems
Attn: Jon Conner
P.O. Box 849
Mesa, Arizona 85211

1 Wright Laboratory
WL/MNMW Bldg. 13
Attn: William Cook
Eglin AFB, FL 32542-5434

1 Dominica
Attn: Nancy Winfree
9813 Admiral Dewey
Albuquerque, NM 87111

1 U. S. Army Natick Research and Development Center
SATNC-IB
Attn: Philip Cunniff
Kansas Street
Natick, MA 01760-5019

1 University of Illinois
NCSA
Attn: LeRay Dandy
Urbana Champaign, IL

1 TASC, Inc.
Attn: Charles Drutman
5500 Walkers Brook Drive
Reading, MA 01940

1 The Ensign-Bickford Company
Attn: Kevin Duprey
660 Hopmeadow Street
Simsbury, CT 06070-0483

1 Advatech Pacific Inc.
Attn: Jay Ebersohl
PO Box 1376
San Bernardino, CA 92402-1376

1 Foils Engineering
Attn: Marshall B. Eck
25731 Ridge Road
Damascus, MD 20872

1 Enig Associates, Inc.
Attn: Julius W. Enig
11120 New Hampshire Ave., Suite 500
Silver Spring, MD 20904-2633

1 General Dynamics
Attn: James Eridon
Mail Zone 439-01-07
P. O. Box 2094
Warren, MI 48090-2094

1 Logicon RDA
Attn: William R. Espander
P.O. Box 9377
Albuquerque, NM 87119-9377

1 University of Texas
Department of Mechanical Engineering
ETC 5.160
Attn: Eric P. Fahrenthold
Austin, TX 78712

1 Lockheed Martin Tactical Defense Systems
Attn: Gregg K. Fenton
1210 Massillon Road
Akron, OH 44315-0001

1 Texas A&M University
Nuclear Engineering Dept.
Zachry Building, Room 129
Attn: Bruce L. Freeman
Mail Stop 3133
College Station, Texas 77843-3133

1 UDLP MS M443
Attn: Jerome Glaser
4800 East River Road
Minn., MN 55421

1 Naval EOD
Technology Division
Code 6021A
Attn: Richard Gold
Indian Head, MD 20640-5070

1 Washington State University
Department of Physics
Shock Dynamics Laboratory
Attn: Y. M. Gupta
Pullman, WA 99164-2814

1 S-Cubed
Attn: Gerry Gurtman
P.O. Box 1620
La Jolla, Ca.92037

1 Lockheed Martin
Attn: Allen Hagan
MP 544
5600 Sand Lake Road
Orlando, FL 32819-8907

1 Naval Facilities Service Center
Waterfront Structures Division
Attn: Kevin Hager
560 Center Drive
Port Hueneme, CA 93043

1 Thiokol Corporation
Science & Engineering Division
Attn: Robert L. Hatch
Mailstop 244
P. O. Box 707
Brigham City, Utah 84302-0707

1 Lockheed Martin Vought Systems
Senior Engineering Specialist - Lethality
Attn: Kenneth W. Havens
P.O. Box 650003 M/S EM-36
Dallas, TX 75265-0003

1 NASA Langley Research Center
Attn: Scott A. Hill
Mail Stop 431
Hampton, VA 23681-0001

1 Network Computing Services, Inc.
AHPCRC
Attn: Tim Holmquist
1200 Washington Avenue South
Minneapolis, MN 55415

1 University of Washington
Department of Aeronautics and Astronautics
Attn: Keith A. Holsapple, FS10
Seattle, WA 98195

1 Boeing Corporation
Attn: Kevin Housen
MS 8H-05, 18.03
P. O. Box 3999
Seattle, WA 98124

1 U. S. Army MICOM
Attn: Scott Howard
Bldg. 5400, Room B-314
Redstone Arsenal, AL 35898-5247

1 AFRL/MNMW
Attn: Dr. Molly Hughes
101 W. Eglin Blvd. Ste. 135
Eglin AFB, FL 32542-6810

1 Texas Tech University
Department of Mechanical Engineering
Attn: Darryl James
Box 41021
Lubbock, TX 79409-1021

1 Network Computing Services, Inc.
AHPCRC
Attn: Gordon R. Johnson
1200 Washington Avenue South
Minneapolis, MN 55415

1 USA CRREL
Attn: Jerome B. Johnson
PO Box 35170 (Building 4070)
Ft. Wainwright, AK 99701

1 IIT Industries
Attn: Sheldon Jones
P. O. Box 15012
Colorado Springs, CO 80935-5012

15 Kerley Technical Services
Attn: Gerald I. Kerley, Consultant
P.O. Box 709
Appomattox, VA 24522-0709

1 NASA Johnson Space Center
Attn: Justin H. Kerr
Mail Code SN3
Houston, TX 77058

1 Rockwell International Corp.
Rocketdyne Division
Attn: Dennis W. Kneff
6633 Canoga Avenue
Canoga Park, CA 91304

1 Pantex
Attn: Kurtis Kuhrts
Building 11-2
P. O. Box 30020
Amarillo, TX 79177

1 ACTA
Attn: Ronald Lambert
Building 7015, Section 3C
Vandenberg AFB, CA 93437

1 NMSU
Department of Mechanical Engineering
Department 3450
Attn: Leslie, Ian H.
Box 30001
Las Cruces, NM 88003

1 The University of Texas at Austin
Institute for Advanced Technology
Attn: David Littlefield
4030-2 Braker Lane
Austin, TX 78759-5329

9 Los Alamos National Laboratory
Attn: J. Boettger, MS B221
R. Gustavsen, MS P952
R. S. Hixson, MS P952
B. L. Holian, MS J569
J. D. Johnson, MS B221
J. E. Kennedy, MS P950
J. Richey, MS B214
S. Sheffield, MS P952
Yasuyuki Horie, MS D413 X-7
Doug Faux, MS L-140
M. Gerassimenko, MS L-183
Mail Station 5000
P.O. Box 1663
Los Alamos, NM 87545

1 Boeing North America/Rocketdyne Division
Attn: N. A. Louie
Mail Stop EB63
PO Box 7922
Canoga Park, CA 91309-7922

1 Tracor Aerospace Inc.
Mine/Countermine Division
Attn: Mark Majerus
1400 Peoples Plaza, Suite 233
Newark, DE 19702

1 Lockheed Martin Missiles Space
Attn: Erik Matheson
Organization V2-10 Building 157
P. O. Box 3504
Sunnyvale, CA 94089-3504

1 Air Force Institute of Technology/ENP
Attn: Kirk A. Mathews
2950 P Street -- Bldg 640
Wright-Patterson AFB, OH 45433-7765

1 Naval Surface Warfare Center
Code 614
Attn: John McKirgan
9500 MacArthur Blvd.
West Bethesda, MD 20817-5700

1 PL/WSSD
Attn: David F. Medina
Kirtland AFB, NM 87117-6008

1 University of Arizona
Professor of Planetary Science
Attn: H. J. Melosh
Tucson, AZ 85721

1 US Army Space & Missile Defense Command
Attn: Robert Becker, SMDC-TC-WL
PO Box 1500
Huntsville, AL 35807-3801

1 AFRL/MNAC
Attn: Kenneth B. Milligan
101 West Eglin Blvd.
Eglin AFB, FL 32542-6810

1 Timothy W. Moore
PO Box 12273
Huntsville, AL 35815

6 Naval Air Warfare Center
Attn: E. Cykowski, C2746
J. Gill
J. Kandell
A. Lindfors
K. Minnick, C3261
P. J. Miller
1 Administrative Circle
China Lake, CA 93555

8 Naval Surface Warfare Center
Dahlgren Division
Attn: J. R. Cogar, G22
R. K. Garrett, Jr, G24
M. Hobson, G22
W. Holt, G24
W. Mock, Jr., G24
D. F. Robinson, G24
D. Vavrick, G22
L. T. Wilson, G24
17320 Dahlgren Rd.
Dahlgren, VA 22448

2 Naval Surface Warfare Center
Indian Head Division
Attn: J. Burns, 4220
G. T. Sutherland, 9230E
101 Strauss Avenue
Indian Head, MD 20640-5035

1 Concurrent Technologies Corp.
Attn: Glenn Nickodemus
1450 Scalp Ave.
Johnston, PA 15904

1 International Research Associates
Attn: Dennis L. Orphal
4450 Black Ave., Suite E
Pleasanton, CA 94566

1 UTEP
FAST Center for Structural Integrity of Aerospace Systems
Attn: Roberto A. Osegueda
500 West University Avenue
El Paso, TX 79968

1 The Aerospace Corporation
Attn: R. B. Pan
M/S: M4/920
P. O. Box 92957
Los Angeles, CA 90009-2957

1 Wright Laboratory/Armament Directorate
WL/MNSA
Attn: Bruce C. Patterson
Eglin AFB, FL 32542-5434

1 Brookhaven National Laboratory
National Synchrotron Light Source
Attn: Paul A. Montanez
Bldg. 725D
Upton, NY 11973-5000

1 NASA Langley Research Center
Attn: ,Carl Poteet
MS 396
Hampton, VA 23681-0001

1 University of Notre Dame
Department of Aerospace and Mechanical Engineering
Attn: Joseph M. Powers
372 Fitzpatrick Hall of Engineering
Notre Dame, Indiana 46556-5637

1 Rockwell Science Center
Attn: S. V. Ramakrishnan
1049 Camino Dos Rios
Thousand Oaks, CA 9136

1 KTech
Attn: Doug Reeder
901 Pennsylvania Ave., N.E.
Albuquerque, NM 87110

1 AlliedSignal
Federal Manufacturing and Technology Group
Attn: Ted Rupp
3500 Trinity Dr., Suite C3
Los Alamos, NM 87544

1 NSWC-IH
Code 90
Attn: Thomas P. Russell
101 Strauss
Indian Head, MD 20640

1 AZ Technologies
Attn: Craig Schmitz
4901 Corporate Drive, Suite 101
Huntsville, AL 35805

1 University of Alabama in Huntsville
University of Missouri-Rolla
CE Department
Attn: William Schonberg
Rolla, MO 65409

1 U. S. Army Corps Engineers
CEMRO-ED-SH
Attn: William Seipel
215 North 17th Street
Omaha, NE 68102

1 LM Aeronautical Systems Company
Department 73-CC2, Zone 0648
Attn: Bharat M. Shah
86 South Cobb Drive
Marrietta, GA 30063

1 California Institute of Technology
Graduate Aeronautical Laboratories
Associate Professor of Aeronautics
Attn: Joseph E. Shepherd
MS 105-50
Pasadena, CA 91125

1 Sverdrup Technology Inc., AEDC Group
Attn: Mark Smith
740 Fourth Street
Arnold AFB, TN 37389-6001

1 SAIC
Attn: Wilford Smith
4901 Olde Towne Parkway, Suite 200
Marietta, GA 30068

1 Air Force Research Laboratory
Attn: Guy C. Spitale
3550 Aberdeen Ave SE
Kirtland AFB, NM 87117-5776

1 Alliant TechSystems
Attn: Frederick Stecher
600 2nd Street NE (MN11-2720)
Hopkins, MN 55343

1 California Institute of Technology
Seismological Laboratory 252-21
Attn: Sarah T. Stewart-Mukhopadhyay
Pasadena, CA 91125

1 Applied Research Associates
Attn: David J. Stevens
1846 Lockhill-Selma Road, Suite 107
San Antonio, TX 78213

1 Raytheon TI Systems
Warhead/Fuze Systems Manager
Attn: Stoney Stonebraker
PO Box 405 MS 3468
Lewisville, TX 75067

1 Dynetics
Attn: Allen Stults
P.O. Drawer B
1000 Explorer Blvd.
Huntsville, AL 35814-5050

1 Plattsburgh State University
Department of Physics
Attn: Paul P. Szydlik
101 Broad Street
Plattsburg, NY 12901-2681

1 46 OG/OGM
Project Engineer
Attn: Ian S. Talbot
205 W. D Ave Suite 241
Eglin AFB, FL 32542-6866

1 Oak Ridge National Laboratory
Attn: Rusi Taleyarkhan
MS 8058
P. O. Box 2009
Oak Ridge, TN 37831-8058

1 James L. Thompson
Attn: AMSTA-RSS,
Warren, MI 48397-5000

1 U. S. Army Engineering Division
CEHND-ED-SY
Attn: John Tipton
P.O. Box 1600
Huntsville, AL 35807-4301

1 Battelle Memorial Institute
Attn: Dale Trott
201-2693
505 King Ave.
Columbus, OH 43201-2693

8 University of California
Lawrence Livermore National Laboratory
Attn: R.Cauble, MS L-041
N. C. Holmes, MS L-050
D. Maiden, MS L-010
B. Moran, MS L-170
R.M. More, MS L-321
W. J. Nellis, MS L-050
P. C. Souers, MS L-282
D. A. Young, MS L-299
7000 East Ave.
P.O. Box 808
Livermore, CA 94550

10 U.S. Army Research Laboratory (10)
Attn: G. Filbey, Jr., AMSRL-WT-TA
F. Gregory
A. D. Gupta
K. D. Kimsey, AMSRL-WT-TC
P. Kingman, AMSRL-WT-TD
R. Lottero, AMSRL-WT-TB
H. Meyer, Jr., AMSRL-WT-TA
A. Rajendian, SLCBR-TC-AR
D. Scheffler, SLCBR-TB-P
J. Starkenberg
D. Dandekar
P.O. Box 334, Main Station
Aberdeen Proving Ground, MD 21005-5066

1 Southwest Research Institute
Attn: James Walker
P. O. Drawer 28510
San Antonio, TX 78228-0510

1 CIA/OSWR
Attn: John Walton
Washington, DC 20505

1 Military Technology, Inc.
Attn: Mitchell D. White
6767 Old Madison Pike NW
Building 2, Suite 200
Huntsville, AL 35806

1 Lockheed Martin Shunk Works
Department 2512
Attn: Dewey Wong
Building 611
Palmdale, CA 93599

1 Hughes Aircraft Company
Radar Systems Group
RE/R2/V524
Attn: T. E. Wong
P.O. Box 92426
Los Angeles, CA 90009-2426

1 Svedrup Technology
Attn: Nick Yakaboski
Building 260
PO Box 1935
Eglin AFB, FL 32542

1 Combustion Research and
Flow Technology, Inc.
Attn: Brian J. York
PO Box 1150
Dublin, PA 18917

1 Naval Research Laboratory
Attn: F. Zerilli
Washington,DC 20375

1	MS	0130	J. Polito, 1200
1		0318	M. B. Boslough, 9212
1		0321	W. J. Camp, 9200
1		0819	E. A. Boucheron, 9231
1		0819	K. G. Budge, 9231
1		0819	D. E. Carroll, 9231
1		0819	C. J. Garasi, 9231
1		0819	A. C. Robinson, 9231
1		0819	R. M. Summers, 9231
1		0819	T. G. Trucano, 9211
1		0819	J. R. Weatherby, 9231
1		0819	M. K. Wong, 9231
1		0820	P. Chavez, 9232
1		0820	R. M. Brannon, 9232
1		0820	R. E. Cole, 9232
1		0820	D. Crawford, 9232
1		0820	A. V. Farnsworth, 9232
1		0820	M. E. Kipp, 9232
1		0820	S. A. Silling, 9232
1		0820	P. A. Taylor, 9232
1		0834	A. C. Ratzel, 9112
1		0836	E. S. Hertel, 9116
1		0836	M. R. Baer, 9100
1		0836	M. Hobbs, 9116
1		1033	J. L. Wise, 6211
1		1168	M. D. Furnish, 1612
1		1168	C. Deeney, 1612
1		1178	Doug Bloomquist, 1630
1		1181	J. R. Asay, 1610
10		1181	L. C. Chhabildas, 1610
1		1181	M. Knudson, 1610

1	1181	W. D. Reinhart, 1610
1	1181	C. A. Hall, 1610
1	1181	J. P. Davis, 1610
1	1185	Dan Kelly, 15417
1	1185	Bob Weir, 15417
1	1185	R. Dukart, 15417
1	1186	Jeff Lawrence, 1674
1	1190	J. P. Quintenz, 1600
1	1191	Keith Matzen, 1670
1	1194	D. H. McDaniel, 1640
1	9042	L. E. Voelker, 8742
1	9042	J. J. Dike, 8743
1	9042	M. Horstemeyer, 8743
2	0899	Technical Library,9616
1	0612	Review and Approval Desk,
1	4912	for DOE/OSTI
1	9018	Central Technical Files, 8945-1